3. Suzuki K, Kono T. Evidence that insulin causes translocation of glucose transport activity to the plasma membrane from an intracellular storage site. Proc Natl Acad Sci U S A 1980;77:2542–2545.
4. Cushman SW,Wardzala LJ. Potential mechanism of insulin action on glucose transport in the isolated rat adipose cell. J Biol Chem 1980;255:4758–4762.
5. Saltiel AR, Kahn CR. Insulin signalling and the regulation of glucose and lipid metabolism. Nature 2001;414:799–806.
6. Watson RT, Kanzaki M, Pessin JE. Regulated membrane trafficking of the insulin-responsive glucose transporter 4 in adipocytes. Endocr Rev 2004;25:177–204.
7. Livingstone C, James DE, Rice JE, Gould GW. Compartment ablation analysis of the insulin-responsive glucose transporter (GLUT4) in 3T3L1 adipocytes. Biochem J 1996;315:487–495.
8. Fujita H, Hatakeyama H, Watanabe TM, Sato M, Higuchi H, Kanzaki M. Identification of three distinct functional sites of insulin-mediated GLUT4 trafficking in adipocytes using quantitative single molecule imaging. Mol Biol Cell 2010;21:2721–2731.
9. Shi J, Kandror KV. Sortilin is essential and sufficient for the formation of Glut4 storage vesicles in 3T3-L1 adipocytes. Dev Cell 2005;9:99–108.
10. Kandror KV, Yu L, Pilch PF. The major protein of GLUT4-containing vesicles, gp160, has aminopeptidase activity. J Biol Chem 1994;269:30777–30780.
11. Martin S, Tellam J, Livingstone C, Slot JW, Gould GW, James DE. The glucose transporter (GLUT-4) and vesicle-associated membrane protein-2 (VAMP-2) are segregated from recycling endosomes in insulin-sensitive cells. J Cell Biol 1996;134:625–635.
12. Lin BZ, Pilch PF, Kandror KV. Sortilin is a major protein component of Glut4-containing vesicles. J Biol Chem 1997;272:24145–24147.
13. Jedrychowski MP, Gartner CA, Gygi SP, Zhou L, Herz J, Kandror KV, Pilch PF. Proteomic analysis of GLUT4 storage vesicles reveals LRP1 to be an important vesicle component and target of insulin signaling. J Biol Chem 2010;285:104–114.
14. Martin S, Rice JE, Gould GW, Keller SR, Slot JW, James DE. The glucose transporter GLUT4 and the aminopeptidase vp165 colocalise in tubulo-vesicular elements in adipocytes and cardiomyocytes. J Cell Sci 1997;110:2281–2291.
15. Malide D, Dwyer NK, Blanchette-Mackie EJ, Cushman SW. Immunocytochemical evidence that GLUT4 resides in a specialized translocation post-endosomal VAMP2-positive compartment in rat adipose cells in the absence of insulin. J Histochem Cytochem 1997;45:1083–1096.
16. Shewan AM, van Dam EM, Martin S, Luen TB, Hong W, Bryant NJ, James DE. GLUT4 recycles via a trans-Golgi network (TGN) subdomain enriched in Syntaxins 6 and 16 but not TGN38: involvement of an acidic targeting motif. Mol Biol Cell 2003;14:973–986.
17. Huang S, Czech MP. The GLUT4 glucose transporter. Cell Metab 2007;5:237–252.
18. Slot JW, Geuze HJ, Gigengack S, Lienhard GE, James DE. Immunolocalization of the insulin regulatable glucose transporter in brown adipose tissue of the rat. J Cell Biol 1991;113:123–135.
19. Martin S, Millar CA, Lyttle CT, Meerloo T, Marsh BJ, Gould GW, James DE. Effects of insulin on intracellular GLUT4 vesicles in adipocytes: evidence for a secretory mode of regulation. J Cell Sci 2000;113:3427–3438.
20. Ramm G, Slot JW, James DE, Stoorvogel W. Insulin recruits GLUT4 from specialized VAMP2-carrying vesicles as well as from the dynamic endosomal/trans-Golgi network in rat adipocytes. Mol Biol Cell 2000;11:4079–4091.
21. Rice KM, Lienhard GE, Garner CW. Regulation of the expression of pp160, a putative insulin receptor signal protein, by insulin, dexamethasone, and 1-methyl-3-isobutylxanthine in 3T3-L1 adipocytes. J Biol Chem 1992;267:10163–10167.
22. Thoidis G, Kotliar N, Pilch PF. Immunological analysis of GLUT4-enriched vesicles. Identification of novel proteins regulated by insulin and diabetes. J Biol Chem 1993;268:11691–11696.
23. Govers R, Coster AC, James DE. Insulin increases cell surface GLUT4 levels by dose dependently discharging GLUT4 into a cell surface recycling pathway. Mol Cell Biol 2004;24:6456–6466.
24. Karylowski O, Zeigerer A, Cohen A, McGraw TE. GLUT4 is retained by an intracellular cycle of vesicle formation and fusion with endosomes. Mol Biol Cell 2004;15:870–882.
25. Ariga M, Nedachi T, Katagiri H, Kanzaki M. Functional role of sortilin in myogenesis and development of insulin-responsive glucose transport system in C2C12 myocytes. J Biol Chem 2008;283:10208–10220.
26. Tsuchiya Y, Hatakeyama H, Emoto N, Wagatsuma F, Matsushita S, Kanzaki M. Palmitate-induced down-regulation of sortilin and impaired GLUT4 trafficking in C2C12 myotubes. J Biol Chem 2010;285:34371–34381.
27. Morris NJ, Ross SA, Lane WS, Moestrup SK, Petersen CM, Keller SR, Lienhard GE. Sortilin is the major 110-kDa protein in GLUT4 vesicles from adipocytes. J Biol Chem 1998;273:3582–3587.
28. Cramer JF, Gustafsen C, Behrens MA, Oliveira CL, Pedersen JS, Madsen P, Petersen CM, Thirup SS. GGA autoinhibition revisited. Traffic 2010;11:259–273.
29. Nielsen MS, Madsen P, Christensen EI, Nykjaer A, Gliemann J, Kasper D, Pohlmann R, Petersen CM. The sortilin cytoplasmic tail conveys Golgi-endosome transport and binds the VHS domain of the GGA2 sorting protein. Embo J 2001;20:2180–2190.
30. McCormick PJ, Dumaresq-Doiron K, Pluviose AS, Pichette V, Tosato G, Lefrancois S. Palmitoylation controls recycling in lysosomal sorting and trafficking. Traffic 2008;9:1984–1997.
31. Bonifacino JS, Hurley JH. Retromer. Curr Opin Cell Biol 2008;20:427–436.
32. Lieu ZZ, Derby MC, Teasdale RD, Hart C, Gunn P, Gleeson PA. The golgin GCC88 is required for efficient retrograde transport of cargo from the early endosomes to the trans-Golgi network. Mol Biol Cell 2007;18:4979–4991.
33. Jing J, Junutula JR, Wu C, Burden J, Matern H, Peden AA, Prekeris R. FIP1/RCP binding to Golgin-97 regulates retrograde transport from recycling endosomes to the trans-Golgi network. Mol Biol Cell 2010;21:3041–3053.
34. Okada T, Kawano Y, Sakakibara R, Hazeki O, Ui M. Essential role of phophatidylinositol 3-kinase in insulin-induced glucose transport and antilypolysis in rat adipocytes. Studies with a selective inhibitor wortmannin. J Biol Chem 1994;269:3568–3573.
35. Ramm G, Larance M, Guilhaus M, James DE. A role for 14-3-3 in insulin-stimulated GLUT4 translocation through its interaction with the RabGAP AS160. J Biol Chem 2006;281:29174–29180.
36. Kandror K, Pilch PF. Identification and isolation of glycoproteins that translocate to the cell surface from GLUT4-enriched vesicles in an insulin-dependent fashion. J Biol Chem 1994;269:138–142.
37. Coster AC, Govers R, James DE. Insulin stimulates the entry of GLUT4 into the endosomal recycling pathway by a quantal mechanism. Traffic 2004;5:763–771.
38. Martin OJ, Lee A, McGraw TE. GLUT4 distribution between the plasma membrane and the intracellular compartments is maintained by an insulin-modulated bipartite dynamic mechanism. J Biol Chem 2006;281:484–490.
39. Blot V, McGraw TE. Molecular mechanisms controlling GLUT4 intracellular retention. Mol Biol Cell 2008;19:3477–3487.
40. Martin S, Reaves B, Banting G, Gould GW. Analysis of the co-localization of the insulin-responsive glucose transporter (GLUT4) and the trans Golgi network marker TGN38 within 3T3-L1 adipocytes. Biochem J 1994;300:743–749.
41. Jordens I, Molle D, Xiong W, Keller SR, McGraw TE. Insulin-regulated aminopeptidase is a key regulator of GLUT4 trafficking by controlling the sorting of GLUT4 from endosomes to specialized insulin-regulated vesicles. Mol Biol Cell 2010;21:2034–2044.
42. Pessin JE, Saltiel AR. Signaling pathways in insulin action: molecular targets of insulin resistance. J Clin Invest 2000;106:165–169.
43. Hoehn KL, Hohnen-Behrens C, Cederberg A, Wu LE, Turner N, Yuasa T, Ebina Y, James DE. IRS1-independent defects define major nodes of insulin resistance. Cell Metab 2008;7:421–433.
44. Xiong W, Jordens I, Gonzalez E, McGraw TE. GLUT4 is sorted to vesicles whose accumulation beneath and insertion into the plasma membrane are differentially regulated by insulin and selectively affected by insulin resistance. Mol Biol Cell 2010;21:1375–1386.
45. Kaddai V, Jager J, Gonzalez T, Najem-Lendom R, Bonnafous S, Tran A, Le Marchand-Brustel Y, Gual P, Tanti JF, Cormont M. Involvement of TNF-alpha in abnormal adipocyte and muscle sortilin expression in obese mice and humans. Diabetologia 2009;52:932–940.
46. Musunuru K, Strong A, Frank-Kamenetsky M, Lee NE, Ahfeldt T, Sachs KV, Li X, Li H, Kuperwasser N, Ruda VM, Pirruccello JP,

Muchmore B, Prokunina-Olsson L, Hall JL, Schadt EE et al. From noncoding variant to phenotype via SORT1 at the 1p13 cholesterol locus. Nature 2010;466:714–719.
47. Kjolby M, Andersen OM, Breiderhoff T, Fjorback AW, Pedersen KM, Madsen P, Jansen P, Heeren J, Willnow TE, Nykjaer A. Sort1, encoded by the cardiovascular risk locus 1p13.3, is a regulator of hepatic lipoprotein export. Cell Metab 2010;12:213–223.
48. Perera HK, Clarke M, Morris NJ, Hong W, Chamberlain LH, Gould GW. Syntaxin 6 regulates Glut4 trafficking in 3T3-L1 adipocytes. Mol Biol Cell 2003;14:2946–2958.
49. Bose A, Guilherme A, Huang S, Hubbard AC, Lane CR, Soriano NA, Czech MP. The v-SNARE Vti1a regulates insulin-stimulated glucose transport and Acrp30 secretion in 3T3-L1 adipocytes. J Biol Chem 2005;280:36946–36951.
50. Shi J, Kandror KV. The luminal Vps10p domain of sortilin plays the predominant role in targeting to insulin-responsive Glut4-containing vesicles. J Biol Chem 2007;282:9008–9016.
51. Shi J, Huang G, Kandror KV. Self-assembly of Glut4 storage vesicles during differentiation of 3T3-L1 adipocytes. J Biol Chem 2008;283:30311–30321.
52. Liu LB, Omata W, Kojima I, Shibata H. The SUMO conjugating enzyme Ubc9 is a regulator of GLUT4 turnover and targeting to the insulin-responsive storage compartment in 3T3-L1 adipocytes. Diabetes 2007;56:1977–1985.
53. Hashiramoto M, James DE. Characterization of insulin-responsive GLUT4 storage vesicles isolated from 3T3-L1 adipocytes. Mol Cell Biol 2000;20:416–427.
54. Ross SA, Keller SR, Lienhard GE. Increased intracellular sequestration of the insulin-regulated aminopeptidase upon differentiation of 3T3-L1 cells. Biochem J 1998;330:1003–1008.
55. Waters MG, Pfeffer SR. Membrane tethering in intracellular transport. Curr Opin Cell Biol 1999;11:453–459.
56. Drin G, Morello V, Casella JF, Gounon P, Antonny B. Asymmetric tethering of flat and curved lipid membranes by a golgin. Science 2008;320:670–673.
57. Czech MP, Chawla A, Wook CW, Buxton J, Armoni M, Tang W, Joly M, Corvera S. Exofacial epitope-tagged glucose transporter chimeras reveal COOH-terminal sequences governing cellular localization. J Cell Biol 1993;123:127–135.
58. Verhey KJ, Yeh JI, Birnbaum MJ. Distinct signals in the GLUT4 glucose transporter for internalization and for targeting to an insulin-responsive compartment. J Cell Biol 1995;130:1071–1079.
59. Li LV, Bakirtzi K, Watson RT, Pessin JE, Kandror KV. The C-terminus of GLUT4 targets the transporter to the perinuclear compartment but not to the insulin-responsive vesicles. Biochem J 2009;419: 105–112. 1.
60. Barr FA. A novel Rab6-interacting domain defines a family of Golgi-targeted coiled-coil proteins. Curr Biol 1999;9:381–384.
61. Lu L, Hong W. Interaction of Arl1-GTP with GRIP domains recruits autoantigens Golgin-97 and Golgin-245/p230 onto the Golgi. Mol Biol Cell 2003;14:3767–3781.
62. Hesse D, Hommel A, Jaschke A, Moser M, Bernhardt U, Zahn C, Kluge R, Wittschen P, Gruber AD, Al-Hasani H, Joost HG, Schurmann A. Altered GLUT4 trafficking in adipocytes in the absence of the GTPase Arfrp1. Biochem Biophys Res Commun 2010;394:896–903.
63. Shin HW, Kobayashi H, Kitamura M, Waguri S, Suganuma T, Uchiyama Y, Nakayama K. Roles of ARFRP1 (ADP-ribosylation factor-related protein 1) in post-Golgi membrane trafficking. J Cell Sci 2005;118:4039–4048.
64. Zahn C, Hommel A, Lu L, Hong W, Walther DJ, Florian S, Joost HG, Schurmann A. Knockout of Arfrp1 leads to disruption of ARF-like1 (ARL1) targeting to the trans-Golgi in mouse embryos and HeLa cells. Mol Membr Biol 2006;23:475–485.
65. Luke MR, Kjer-Nielsen L, Brown DL, Stow JL, Gleeson PA. GRIP domain-mediated targeting of two new coiled-coil proteins, GCC88 and GCC185, to subcompartments of the trans-Golgi network. J Biol Chem 2003;278:4216–4226.
66. Derby MC, van Vliet C, Brown D, Luke MR, Lu L, Hong W, Stow JL, Gleeson PA. Mammalian GRIP domain proteins differ in their membrane binding properties and are recruited to distinct domains of the TGN. J Cell Sci 2004;117:5865–5874.
67. Lock JG, Hammond LA, Houghton F, Gleeson PA, Stow JL. E-cadherin transport from the trans-Golgi network in tubulovesicular carriers is selectively regulated by golgin-97. Traffic 2005;6:1142–1156.
68. Lu L, Tai G, Hong W. Autoantigen Golgin-97, an effector of Arl1 GTPase, participates in traffic from the endosome to the trans-golgi network. Mol Biol Cell 2004;15:4426–4443.
69. Yoshino A, Setty SR, Poynton C, Whiteman EL, Saint-Pol A, Burd CG, Johannes L, Holzbaur EL, Koval M, McCaffery JM, Marks MS. tGolgin-1 (p230, golgin-245) modulates Shiga-toxin transport to the Golgi and Golgi motility towards the microtubule-organizing centre. J Cell Sci 2005;118:2279–2293.
70. Derby MC, Lieu ZZ, Brown D, Stow JL, Goud B, Gleeson PA. The trans-Golgi network golgin, GCC185, is required for endosome-to-Golgi transport and maintenance of Golgi structure. Traffic 2007;8:758–773.
71. Sinka R, Gillingham AK, Kondylis V, Munro S. Golgi coiled-coil proteins contain multiple binding sites for Rab family G proteins. J Cell Biol 2008;183:607–615.
72. Hayes GL, Brown FC, Haas AK, Nottingham RM, Barr FA, Pfeffer SR. Multiple Rab GTPase binding sites in GCC185 suggest a model for vesicle tethering at the trans-Golgi. Mol Biol Cell 2009;20:209–217.
73. Miinea CP, Sano H, Kane S, Sano E, Fukuda M, Peranen J, Lane WS, Lienhard GE. AS160, the Akt substrate regulating GLUT4 translocation, has a functional Rab GTPase activating protein domain. Biochem J 2005;391:87–93.
74. Sano H, Eguez L, Teruel MN, Fukuda M, Chuang TD, Chavez JA, Lienhard GE, McGraw TE. Rab10, a target of the AS160 Rab GAP, is required for insulin-stimulated translocation of GLUT4 to the adipocyte plasma membrane. Cell Metab 2007;5:293–303.
75. Sano H, Kane S, Sano E, Miinea CP, Asara JM, Lane WS, Garner CW, Lienhard GE. Insulin-stimulated phosphorylation of a Rab GTPase-activating protein regulates GLUT4 translocation. J Biol Chem 2003;278:14599–14602.
76. Larance M, Ramm G, Stockli J, van Dam EM, Winata S, Wasinger V, Simpson F, Graham M, Junutula JR, Guilhaus M, James DE. Characterization of the role of the Rab GTPase-activating protein AS160 in insulin-regulated GLUT4 trafficking. J Biol Chem 2005;280:37803–37813.
77. Brewer PD, Romenskaia I, Kanow MA, Mastick CC. Loss of AS160 causes Glut4 to accumulate in compartments that are primed for fusion in basal adipocytes. J Biol Chem 2011;286:26287–26297.
78. Hosaka T, Brooks CC, Presman E, Kim SK, Zhang Z, Breen M, Gross DN, Sztul E, Pilch PF. p115 Interacts with the GLUT4 vesicle protein, IRAP, and plays a critical role in insulin-stimulated GLUT4 translocation. Mol Biol Cell 2005;16:2882–2890.
79. Williams D, Hicks SW, Machamer CE, Pessin JE. Golgin-160 is required for the Golgi membrane sorting of the insulin-responsive glucose transporter GLUT4 in adipocytes. Mol Biol Cell 2006;17:5346–5355.
80. Canuel M, Libin Y, Morales CR. The interactomics of sortilin: an ancient lysosomal receptor evolving new functions. Histol Histopathol 2009;24:481–492.
81. Watson RT, Khan AH, Furukawa M, Hou JC, Li L, Kanzaki M, Okada S, Kandror KV, Pessin JE. Entry of newly synthesized GLUT4 into the insulin-responsive storage compartment is GGA dependent. Embo J 2004;23:2059–2070.
82. Sargeant RJ, Paquet MR. Effect of insulin on the rates of synthesis and degradation of GLUT1 and GLUT4 glucose transporters in 3T3-L1 adipocytes. Biochem J 1993;290:913–919.
83. Brown D, Breton S, Ausiello DA, Marshansky V. Sensing, signaling and sorting events in kidney epithelial cell physiology. Traffic 2009;10:275–284.
84. Kanzaki M, Pessin JE. Insulin-stimulated GLUT4 translocation in adipocytes is dependent upon cortical actin remodeling. J Biol Chem 2001;276:42436–42444.
85. Li Q, Lau A, Morris TJ, Guo L, Fordyce CB, Stanley EF. A syntaxin 1, Galpha(o), and N-type calcium channel complex at a presynaptic nerve terminal: analysis by quantitative immunocolocalization. J Neurosci 2004;24:4070–4081.

Wireless Magnetic Position-Sensing System Using Optimized Pickup Coils for Higher Accuracy

S. Hashi[1], S. Yabukami[2], H. Kanetaka[3], K. Ishiyama[1], and K. I. Arai[4]

[1]Resarch Institute of Electrical Communication, Tohoku University, Sendai 980-8577, Japan
[2]Depertment of Electrical Engineering and Information Technology, Tohoku-Gakuin University, Tagajo 985-8537, Japan
[3]Graduate School of Medical Engineering, Tohoku University, Sendai 980-8575, Japan
[4]The Research Institute for Electric and Magnetic Materials, Sendai 982-0807, Japan

With the aim of improving the detection accuracy of a wireless magnetic position-sensing system using an LC resonant magnetic marker, a pickup coil with an optimal size (10 mm in diameter × 1 mm thick), as calculated by a previous simulation study, was used and tested in this paper. Our study confirmed that positional errors were reduced to a submillimeter order in the area within $y = 120$ mm from the pickup coil array. On the contrary, in the area outside $y = 130$ mm from the pickup coil array, the errors increased by about 0.5–2 mm compared to the results for the previous pickup coil size (25 mm in diameter × 2 mm thick). Regardless of the size of the pickup coil, however, compensation can be made for these positional deviations, including the influence of the mutual inductance between the LC marker and the exciting coil. After application of the compensation process, the detection results were corrected approximately to the actual positions of the LC marker.

***Index Terms*—LC resonant magnetic marker, pickup coil size, position accuracy, wireless magnetic position-sensing system.**

I. Introduction

A MOTION-SENSING technique with an accuracy of better than 1 mm is required for body-motion analysis in medical treatment and health welfare. A wireless magnetic position-detection system is one technique that is effective for such a purpose because it can capture the motion of objects in unseen areas [1]–[7]. To this end, we propose a candidate system using an LC resonant magnetic marker (LC marker) [8], [9]. Previous studies have shown that such a system is capable of repeatable position-detection accuracy of better than 1 mm provided the system has an adequate signal-to-noise (S/N) ratio. However, slight positioning errors of a millimeter order from the actual positions were observed in the local area. To address this problem, an examination by numerical analysis was carried out to clarify the cause of the slight errors in detection and to improve the accuracy of the system [10]. The results indicate that the slight errors in positional accuracy are caused by the influence of the size of the marker and the pickup coils. This is due to the assumption that the marker and the pickup coils are assumed to be an ideal dipole field and number of points, respectively. It is also found that a 10-mm-diameter pickup coil with a wound coil thickness of 1 mm achieves a detection accuracy of better than 0.1 mm [10]. In this paper, therefore, a magnetic position-sensing system using pickup coils of that size is experimentally evaluated.

II. Experiments

A. Configuration of the Position Sensing System

Fig. 1 shows the schematic configuration of the position-sensing system. The system comprises measurement apparatuses and a coil assembly that consists of an exciting coil and a pickup coil array. The exciting coil and the pickup coil array are positioned at a distance of 285 mm from each other. The exciting coil consists of 13 turns of polyester enameled copper wire (PEW) wound around a 390 × 390-mm square acryl frame, and the pickup coil array consists of 25 pickup coils placed at intervals of 45 mm on an acrylic board. Fig. 2(a) and (b) shows the previously used pickup coil and the new pickup coil. The previous pickup coil had 40 turns of PEW wound around an acrylic bobbin 25 mm in diameter and 2 mm thick, and the new one has 100 turns around a bobbin 10 mm in diameter and 1 mm thick. The LC marker consists of a Ni-Zn ferrite core (3 mm in diameter and 10 mm long) with 250 turns of wound coil and a chip capacitor (470 pF), representing an LC series circuit designed for a resonant frequency of 306 kHz.

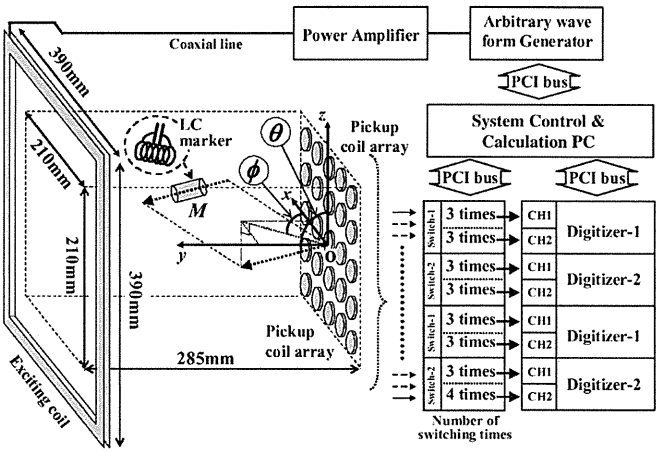

Fig. 1. Schematic diagram of proposed wireless motion-sensing system.

In a previous study, for reference, the procedure of numerical analysis for obtaining the optimal size of the pickup coil is as follows. First, the linkage flux generated by the exciting coil across the marker assumed by the solenoid coil is calculated. Then, the marker coil current is obtained from the induced

Manuscript received February 21, 2011; accepted May 01, 2011. Date of current version September 23, 2011. Corresponding author: S. Hashi (e-mail: shashi@riec.tohoku.ac.jp).

Color versions of one or more of the figures in this paper are available online at http://ieeexplore.ieee.org.

Digital Object Identifier 10.1109/TMAG.2011.2154313

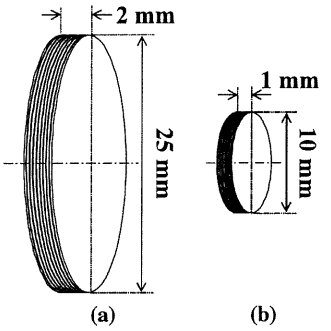

Fig. 2. Dimensions of the pickup coils (figures show only the coil winding part). (a) Diameter: 25 mm; width: 2 mm (used in previous study). (b) Diameter: 10 mm; width: 1 mm (used in this study).

voltage calculated by $d\Phi/dt$ (here, $t = 1/f_r$) as well as the measured impedance of the marker coil. Second, the linkage flux generated by the marker coil across each pickup coil is calculated, and the induced voltage of each pickup coil is obtained. Finally, a calculation of the inverse problem using the obtained induced voltages yields a solution. Here, the averaged magnetic flux of 100 points of a cross section of a coil (both the marker and the pickup coils) is calculated so as to take into consideration the area of the marker and pickup coil. The influence of the coil depth (axial length) also is taken into consideration. The calculation of the magnetic flux is made in accordance with Biot–Savart's law.

B. Position-Sensing Procedure

When voltage is applied to the exciting coil, the LC marker is strongly excited at its resonant frequency by electromagnetic induction. However, the induced electromotive force detected by the pickup coils includes both the electromotive force resulting from the exciting field and that from the LC marker field, as they have the same frequency component. To extract the LC marker contribution, the reference electromotive force, which is called "background voltage" in this paper, is first measured without the LC marker. Next, the electromotive force with the LC marker is measured. The LC marker voltage V_{mk} can then be obtained by subtracting the electromotive force without LC marker from the electromotive force with it.

The position and orientation of the LC marker is calculated by solving an inverse problem, which requires knowing the values of the flux density at more than six known locations in order to determine both the position and orientation of the LC marker as the magnetic flux source (six degrees of freedom). Twenty-five values were used in this study. To solve this problem, the flux density generated from the LC marker is considered to be a magnetic dipole field. Based upon this assumption, the position and orientation of the LC marker is calculated using the nonlinear method of least squares, which are optimized using the Gauss–Newton method [11] (see our previous papers [8] and [9] for details). In this paper, as shown in Fig. 1, the position and orientation of the LC marker are expressed as polar coordinates.

III. Results and Discussion

Position sensing by the LC marker was performed as follows. After positioning the LC marker so that the cylinder axis was parallel to the y-axis, the LC marker was swept from $y = 50$ to 200 mm in 10-mm steps, and from $x = 0$ to 80 mm in 20-mm steps along a grid pattern in the xy plane at $z = 0$ mm. Movement of the LC marker was performed by a precision three-dimensional-axial manual scanner with a positioning accuracy of better than 0.1 mm. In order to make the S/N ratio of both sizes of pickup coils approach the same level, when using the 25-mm-diameter pickup coils, 60 V_{0-p} was applied to the exciting coil. When using the 10-mm-diameter pickup coils, 84 V_{0-p} was applied to it.

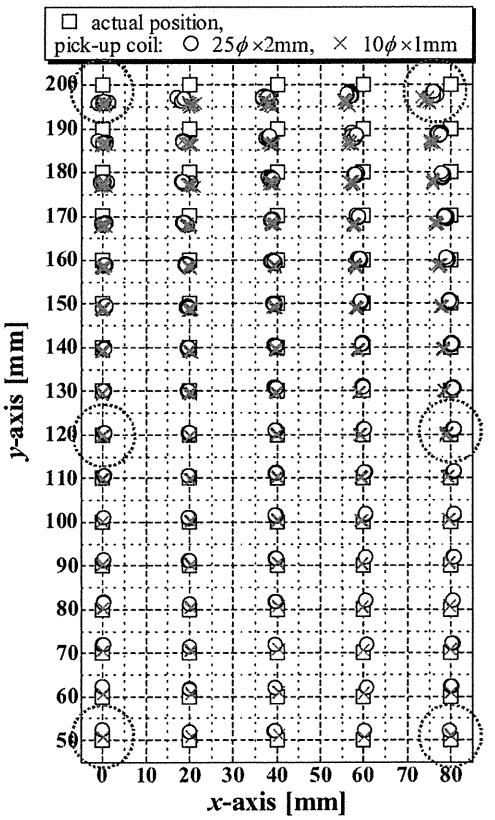

Fig. 3. Position detection results displayed in the xy plane for systems using both sizes of pickup coils.

Fig. 3 shows the experimental results in the xy plane for both sizes of pickup coil. Each point represents 10 measurements at each LC marker position, with squares showing actual position, crosses showing use of the 10-mm-diameter pickup coil, and circles showing use of the 25-mm-diameter pickup coil. Good repeatable accuracy of within 1 mm was obtained at less than $y = 150$ mm. However, as the distance of the LC marker from the pickup coil array increases to beyond 150 mm, the positional deviation between the actual position and the detected position of the LC marker increase, and the scatter of repeatable accuracy is spread due to the drop in the S/N ratio.

From a comparison of the results for both pickup coils, in the area within $y = 120$ mm from the pickup coil array, the detected positions using the 10-mm-diameter pickup coils improved to a millimeter order along the y-axis to the actual positions. On the other hand, the detection results for the area outside $y = 130$ mm became slightly worse than that for the system using the 25-mm-diameter pickup coils.

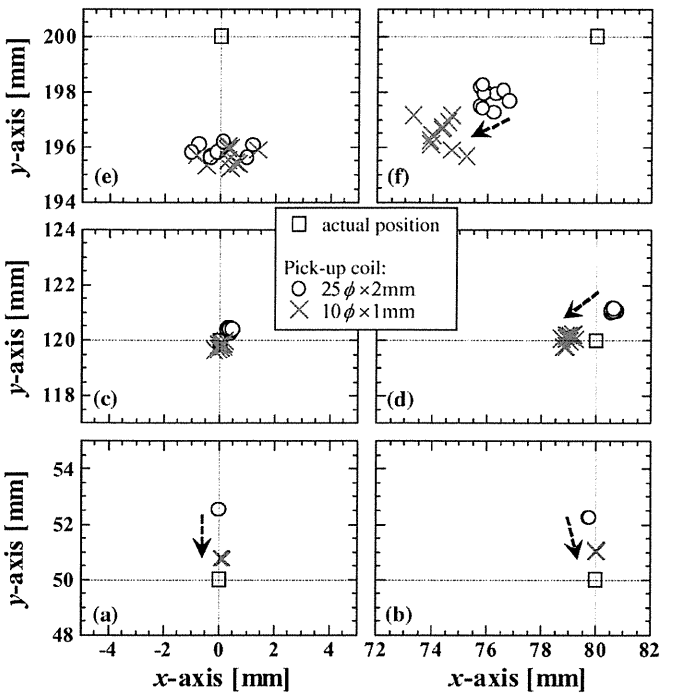

Fig. 4. Position detection results displayed in the xy plane for systems using both size pickup coils. The six points, encircled by dotted lines in Fig. 3, have been magnified. (a) (0, 50, 0). (b) (0, 120, 0). (c) (0, 200, 0). (d) (80, 50, 0). (e) (80, 120, 0). (f) (80, 200, 0).

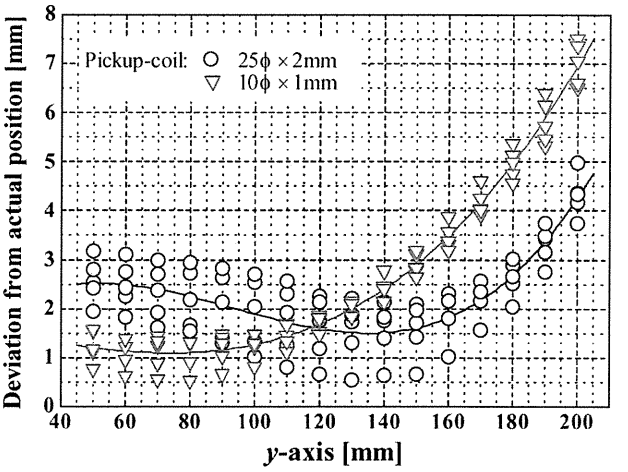

Fig. 5. Relation between detection error and distance of the LC marker from the pickup coil array. Each point shows the difference between the averaged value of 10 measurements and the actual position of the LC marker.

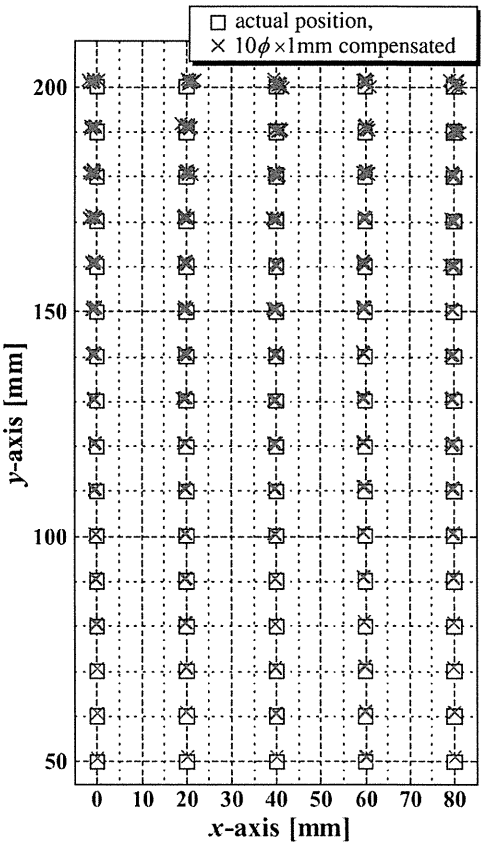

Fig. 6. Compensated detection results made using 10-mm-diameter pickup coils and taking into consideration the mutual inductance between the exciting coil and the LC marker.

According to the simulation result obtained in our previous study taking into consideration the actual sizes of both the LC marker ($\phi 4$ mm $\times$ 10 mm) and the pickup coils ($\phi 25$ mm $\times$ 2 mm), deviations in the millimeter order from the actual position of the LC marker were clearly calculated. In addition, an increase in the tendency to deviation was confirmed in the area within 120 mm from the pickup coil array, the same as in the experiments. The simulation result also indicated that a minimal positional error of less than 0.1 mm can be obtained by using a pickup coil measuring 10 mm in diameter and 1 mm thick [10]. Several points, encircled by dotted lines in Fig. 3, are magnified as shown in Fig. 4(a)–(f) to confirm the difference. Whereas the amount and tendency of the deviation are different for each point, detected positions using 10-mm-diameter pickup coils are improved, ranging from 1 to 3 mm, except for Fig. 4(e) and (f). It was found that the detection error using the 10-mm-diameter pickup coils increased about 0.5–2 mm in the area outside $y = 130$ mm. The relation between the detection error and the distance of the LC marker from the pickup coil array is shown in Fig. 5. Each point shows the difference between the averaged value of 10 measurements and the actual position of the LC marker. The inequality of the detection error is reversed at $y = 120$ mm. The cause of the error tendency is assumed to be the difference in the ratio of solid angles seen from the LC marker with respect to the pickup coil array.

Regardless of the size of the pickup coils, however, compensation can be made for these positional deviations, including the influence of the mutual inductance between the LC marker and the exciting coil. The main factor for the deviations has already been found—the impedance change in the exciting coil due to the resonance of the LC marker disturbing the strength of the exciting field. A compensatory method that takes into consideration this mutual inductance has been established in the process of positional calculation in order to correct the detected position. The compensatory procedure is as follows. The impedance change in the exciting coil resulting from the mutual inductance is calculated by using an equivalent circuit. Next, the electromotive force of the pickup coils within the LC marker is compensated for according to the impedance change. After

the compensation, the inherent position and orientation of the LC marker can be recalculated. The recalculated results for a 10-mm-diameter pickup coil based upon this compensation are shown in Fig. 6. From Fig. 6, the detection results are corrected approximately to the actual positions of the LC marker. However, there are still deviations of a submillimeter order, which are considered to be caused by the volume effect of the coil windings (resulting from the lamination layers of the coil) and machining accuracy resulting from the use of acrylic resin in the coil components.

IV. Conclusion

With the aim of improving the detection accuracy of a wireless magnetic motion-sensing system using an LC resonant magnetic marker, and to confirm the validity of the simulation made in a previous study, the size of the pickup coils were experimentally examined. It was found that the optimal size of the pickup coil, which was deduced by the simulation, improved the detection accuracy of the system to a millimeter order. Therefore, the optimal size of the pickup coils varies as the LC marker size varies. However, slight errors in position detection remain. As mentioned above, the errors are thought to be caused by the volume effect of the coil windings and the machining accuracy of the coil components. In order to realize the system having a positioning accuracy of a submillimeter order, further studies are needed to resolve these issues.

References

[1] F. Grant and G. West, *Interpretation Theory in Applied Geophysics.* New York: McGraw-Hill, 1965, pp. 306–381.

[2] S. V. Marshall, "Vehicle detection using a magnetic field sensor," *IEEE Trans. Veh. Technol.*, vol. VT-27, no. 2, pp. 65–68, May 1978.

[3] W. M. Wynn, C. P. Frahm, P. J. Carroll, R. H. Clark, J. Wellhoner, and M. J. Wynn, "Advanced superconducting gradiometer/magnetometer arrays and a novel signal processing technique," *IEEE Trans. Magn.*, vol. MAG-11, no. 2, pp. 701–707, Mar. 1975.

[4] F. H. Raab, E. B. Blood, T. O. Steiner, and H. R. Jones, "Magnetic position and orientation tracking system," *IEEE Trans. Aerosp. Electron. Syst.*, vol. AES-15, no. 5, pp. 709–718, Sep. 1979.

[5] J. E. Mcfee and Y. Das, "Determination of the parameters of a dipole by measurement of its magnetic field," *IEEE Trans. Antennas Propag.*, vol. AP-29, no. 2, pp. 282–287, Mar. 1981.

[6] J. A. Paradiso, K. Hsiao, J. Stricken, J. Lifton, and A. Adler, "Sensor systems for interactive surfaces," *IBM Syst. J.*, vol. 39, pp. 892–914, 2000.

[7] S. Yabukami, H. Kikuchi, M. Yamaguchi, K. I. Arai, K. Takahashi, Aitagaki, and N. Wako, "Motion capture system of magnetic markers using three-axial magnetic field sensor," *IEEE Trans. Magn.*, vol. 36, no. 5, pp. 3646–3648, Sep. 2000.

[8] S. Yabukami, S. Hashi, Y. Tokunaga, T. Kohno, K. I. Arai, and Y. Okazaki, "A development of position-sensing system for a wireless magnetic marker," *J. Magn. Soc. Jpn.*, vol. 28, pp. 877–885, 2004.

[9] S. Hashi, M. Toyoda, S. Yabukami, K. Ishiyama, Y. Okazaki, K. I. Arai, and H. Kanetaka, "Wireless magnetic motion capture system using multiple LC resonant magnetic markers with high accuracy," *Sensor. Actuat. A, Phys.*, vol. 142, pp. 520–527, 2008.

[10] S. Hashi, S. Yabukami, H. Kanetaka, K. Ishiyama, and K. I. Arai, "Numerical study on the improvement of detection accuracy for a wireless motion capture system," *IEEE Trans. Magn.*, vol. 45, no. 6, pp. 2736–2739, Jun. 2009.

[11] T. Nakagawa and Y. Koyanagi, *Experimental Data Analysis by the Least Square Method.* Tokyo, Japan: Univ. Tokyo Press, 1982, pp. 95–99.

Journal of Medical Engineering & Technology, 2011; 35(6–7): 314–321

ISSN 0309-1902 print/ISSN 1464-522X online
DOI: 10.3109/03091902.2011.591480

informa
healthcare

INNOVATION

Fuzzy FES controller using cycle-to-cycle control for repetitive movement training in motor rehabilitation. Experimental tests with wireless system

Naoto Miura[1]*, Takashi Watanabe[1,2], Satoru Sugimoto[1], Kazunori Seki[3], and Hiroshi Kanai[1,2]

[1]Graduate School of Engineering, Tohoku University, Aoba-ku, Sendai, Japan, [2]Graduate School of Biomedical Engineering, Tohoku University, Graduate school of biomedical engineering, Sendai, Japan and [3]Tohoku University Graduate School of Medicine, Sendai, Japan

A prototype of wireless surface electrical stimulation system combined with the fuzzy FES controller was developed for rehabilitation training with functional electrical stimulation (FES). The developed FES system has three features for rehabilitation training: small-sized electrical stimulator for surface FES, wireless connection between controller and stimulators, and between controller and sensors, and the fuzzy FES controller based on the cycle-to-cycle control for repetitive training. The developed stimulator could generate monophasic or biphasic high voltage stimulus pulse and could output stimulation pulses continuously more than 20 hours with 4 AAA batteries. The developed system was examined with neurologically intact subjects and hemiplegic subjects in knee joint control. The maximum knee joint angle was controlled by regulating burst duration of stimulation pulses by the fuzzy controller. In the results of two experiments of knee extension angle control and knee flexion and extension angle control, the maximum angles reached their targets within small number of cycles and were controlled stably in the stimulation cycles after reaching the target. The fuzzy FES controller based on the cycle-to-cycle control worked effectively to reach the target angle and to compensate difference in muscle properties between subjects. The developed wireless surface FES system would be practical in clinical applications of repetitive execution of similar movements of the limbs for motor rehabilitation with FES.

Keywords: Cycle-to-Cycle Control, Functional Electrical Stimulation, Rehabilitation, Surface Electrical Stimulation, Wireless System

Introduction

Functional electrical stimulation (FES) can be an effective method of assisting or restoring paralyzed motor functions caused by spinal cord injury or cerebrovascular disease. FES has been utilized as an orthotic and therapeutic aid in the rehabilitation of the upper and lower limb motor functions. The therapeutic effects during rehabilitation with FES have been shown to improve muscle strength [1–3] and muscle recruitment [3–4]. The repetitive movement therapy mediated by the electrical stimulation also has the potential to facilitate motor relearning [5].

In motor rehabilitation, goal-oriented repetitive movement training of the paralyzed limbs has been applied. One of the therapeutic effects is motor relearning, which is reacquisition of previously learned motor skills after central nervous system injury. In general, assistance provided by therapists is required to perform repetitive execution of identical or similar movements of the limbs in the rehabilitation training. On the other hand, several large-scale robotic systems have been developed to reduce the workloads for the therapists and improve repeated training for patients [6]. However, these equipments are large and expensive, which are installed in hospitals or rehabilitation centers, and therefore generally unsuitable for home rehabilitation and daily exercise.

For motor rehabilitation with FES, surface electrical stimulation would be useful because of its noninvasive nature. However, the electrical stimulator for surface FES is usually required to generate high stimulation intensity pulses, which leads to an increase of size and power consumption of the stimulator. In addition, wired connection between controller and stimulators and between controller and sensors are sometimes cumbersome and can obstruct the movement of the limb. Therefore, this study focused on miniaturizing the electrical stimulator and on removing the connection code using wireless technology.

In training with FES for rehabilitation, repetitive movements of limbs have to be controlled appropriately by stimulating the relevant muscles. Closed-loop FES control is required to suppress variations of initial position and muscle response, and muscle fatigue in the exercise and to derive benefit from

*Corresponding author. E-mail: naoto.miura@bme.tohoku.ac.jp

the rehabilitation. Tracking control of joint angles of the lower limb is a difficult problem because of nonlinearity and significant time delay, both affecting the responses of the musculoskeletal system to electrical stimulation. For this purpose, the fuzzy FES controller based on the cycle-to-cycle control [7–9] was modified and implemented in the wireless FES system for rehabilitation in this study. The cycle-to-cycle control is a control method for restoring cyclic movements such as gait by using FES [10–11]. Each muscle contraction is controlled by single burst of stimulation pulses with constant pulse amplitude, pulse width and frequency to induce joint movement reaching the target joint angle, in which the stimulation burst duration is regulated.

The purpose of this study is to show the effectiveness of the wireless FES system in which the fuzzy cycle-to-cycle control was implemented for repetitive movement control through control tests with neurologically intact and hemiplegic subjects. In this paper, the wireless surface electrical stimulation system combined with the fuzzy FES controller based on the cycle-to-cycle control was developed. The developed wireless feedback FES system was examined in knee joint control. First, the maximum knee extension angle control stimulating one muscle was performed to find the basic performance of the closed-loop control with the wireless system with neurologically intact subjects and hemiplegic subjects. Then, the maximum knee flexion and extension angle control was performed as a preliminary test of controlling a sequence of movements stimulating two muscles with neurologically intact subjects.

Wireless surface electrical stimulation system

The wireless surface electrical stimulation system consists of three parts: the fuzzy FES controller implemented on the PC, surface electrical stimulator and sensor. For wireless communication between the controller and the stimulator and between the controller and the sensor, a 2.4 GHz wireless transceiver module (WCU-241, K2-denshi) was used. The stimulus data determined by the fuzzy FES controller is transmitted to the stimulator through the wireless transceiver modules. The stimulator generates electrical stimulation pulses immediately after receiving the stimulus data. The data was composed of stimulus voltage, stimulus pulse width and monophasic/biphasic pulse type. The current system can send the stimulus data of up to 4 channels together. The sensor data are digitized by a 10 bit A/D converter with 40 Hz of sampling frequency in the wireless transceiver module and transmitted to the fuzzy FES controller through wireless transceiver module as feedback signal. It is possible to receive the sensor data of up to 4 channels simultaneously. The topology of wireless communication is the point-to-point connection between the controller and the stimulator and between the controller and the sensor, in which the original protocol (the packet consisting of the data of Preamble, Address, Payload and Cyclic Redundancy Check) is used. The bit rate and the latency of the transceiver module are up to 250 kbit/s and about 2 ms, respectively.

Electrical stimulator consists of the wireless transceiver module, the boost converter and the stimulation pulse generator. The boost converter stores electric charges in a tank capacitor and generates high voltage pulse required for the surface electrical stimulation (maximum output voltage: 128 V). The stimulator generates monophasic or biphasic pulse. The maximum stimulation frequency was 520 Hz. In usual FES control, stimulation pulses with a constant stimulation frequency smaller than about 100 Hz are used. High frequency stimulation pulses are sometimes used in research work as a doublet or a triplet [12–13], in which stimulation frequency is about up to 300 Hz. The overall size of the produced stimulator was 70 × 55 × 30 mm. The stimulator's power is supplied by 4 AAA batteries. The electrical stimulator could output stimulation pulses continuously more than 20 hours (monophasic pulse train, frequency: 20 Hz, pulse width: 0.3 ms, pulse amplitude: 80 V).

Outline of fuzzy FES controller based on cycle-to-cycle control

The block diagram of the fuzzy FES control for repetitive movement is shown in figure 1. Output of the fuzzy controller was automatically adjusted by two parameters: error-based output adjustment factor (E-OAF) and sensitivity-based factor (S-OAF). Therefore, the burst duration of stimulation pulses of a current cycle TB[n] is regulated by the following formula:

$$TB[n] = TB[n-1] + \Delta TB[n]$$

where TB[n-1] is the stimulation burst duration for the cycle just before the current one and ΔTB[n] is the output of the fuzzy controller adjusted by the 2 factors.

The fuzzy controller was designed as multi-input single-output (MISO) controller with two inputs of 'error' and

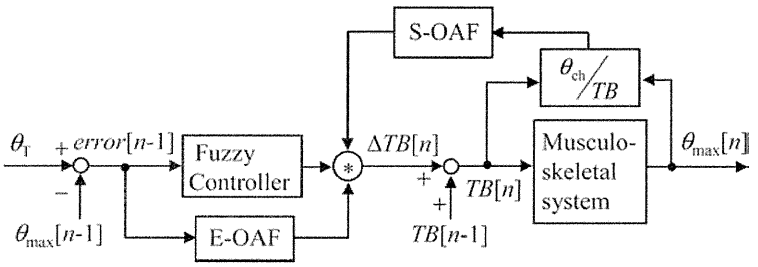

Figure 1. Block diagram of the Fuzzy FES control for repetitive movement. S-OAF, sensitivity-based output adjustment factor; E-OAF, error-based output adjustment factor; θ_T, target maximum angle; θ_{max}, maximum joint angle produced by TB; θ_{ch}, joint angle change produced by TB.

'desired range'. The 'error' was defined as the difference between the target angle and the maximum angle elicited by the burst stimulation pulses. The 'desired range' was defined as the difference between the target angle and the angle at the stimulation onset. The E-OAF is determined by the error of the cycle just before the current cycle, which increases the output value of the controller if the error is large, and decreases if the error is small. The S-OAF is determined by joint angle production ratio that is defined as the ratio of joint angle change to stimulation burst duration, θ_{ch}/TB, which means sensitivity of the muscle to electrical stimulation.

figure 2 shows an example of input and output membership functions of the fuzzy controller for knee extension angle control. Input membership functions were expressed by triangular and trapezoidal fuzzy sets. The membership functions of the 'error' and 'desired range' comprised 7 and 3 linguistic terms, respectively, and that of the output variable was expressed as 11 fuzzy singletons. The membership functions of the E-OAF comprised 5 linguistic terms, and the output variable was expressed as 5 fuzzy singletons. The membership functions of the S-OAF comprised 3 linguistic terms, and the output variable was expressed as 3 fuzzy singletons.

The fuzzy inference was accomplished by using the Mamdani method. Center of gravity (COG) was used in the defuzzification process. Parameter values of the fuzzy controller were determined based on control results and values obtained in our previous studies [7–9], which were fixed during the experiments.

Knee extension angle control with neurologically intact subjects and hemiplegic subjects

Experimental methods

The vastus muscles were stimulated through surface electrodes (SRH5080, SEKISUI PLASTICS), and maximum knee extension angle was controlled by the surface electrical stimulation system (figure 3). Two neurologically intact subjects (subject A, B) and two hemiplegic subjects caused by cerebral apoplexy (subject C: 76-year-old right sided hemiplegic male patient, subject D: 38-year-old left sided hemiplegic male patient) participated in the experiments. Subjects' consent to participate in the experiment was obtained.

The subject seated in the chair (GT-30, OG Giken) and relaxed his legs during experiments. To maintain the sitting position, the trunk of hemiplegic subject was fixed to the chair with band. The sitting position of the neurologically intact subjects was determined by themselves and that of the hemiplegic subject was determined by adjusting the back of the chair in the forward and backward direction for appropriate knee joint movement. Consequently, the initial joint angle was about 65° in neurologically intact subjects and about 80° in hemiplegic subjects (0° means full knee extension). The target angle was 30° (range of knee extension angle was about 35°) for neurologically intact subjects and was 70° or 65° (range of knee extension angle was about 10° or 15°) for hemiplegic subjects. The target angle was determined based on the maximum knee extension angle developed by electrical stimulation. The

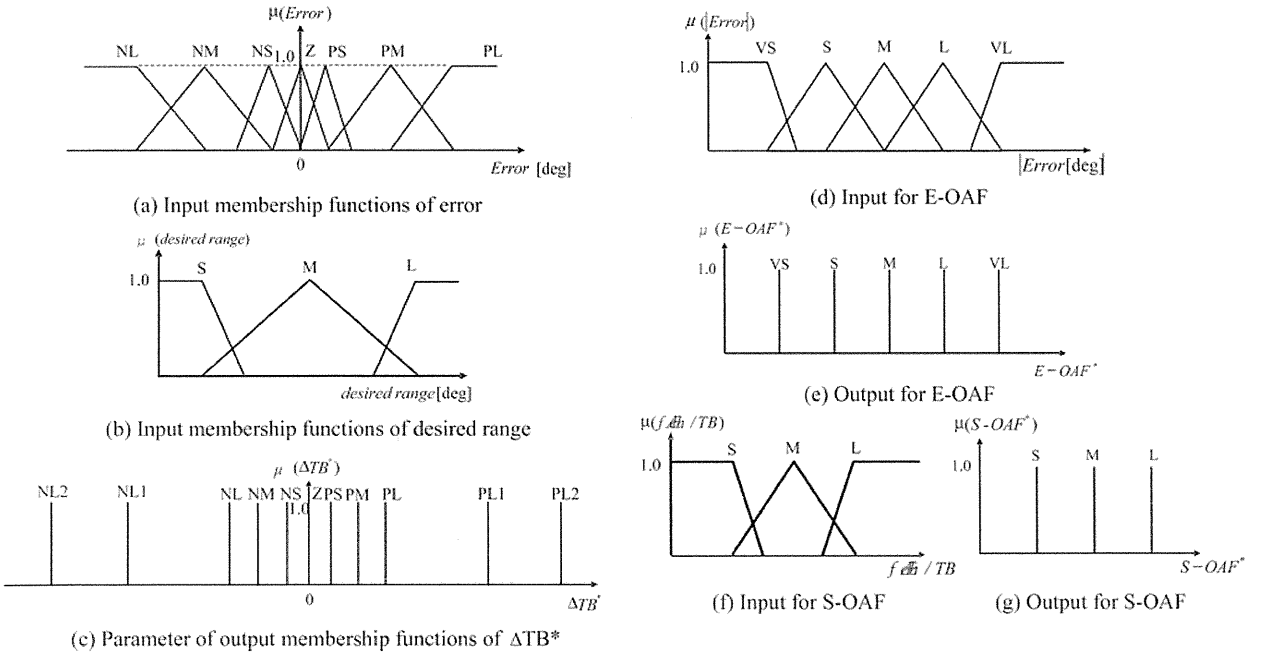

Figure 2. Input/Output membership functions of the fuzzy controller. Input membership functions were expressed by triangular and trapezoidal fuzzy sets. The membership functions of the 'error' and 'desired range' comprised 7 and 3 linguistic terms, respectively, and that of the output variable was expressed as 11 fuzzy singletons. The membership functions of the E-OAF comprised 5 linguistic terms, and the output variable was expressed as 5 fuzzy singletons. The membership functions of the S-OAF comprised 3 linguistic terms, and the output variable was expressed as 3 fuzzy singletons. S, small; M, medium; L, large; NL2, negative large 2; NL1, negative large 1;NL, negative large; NM, negative medium; NS, negative small; Z, zero; PS, positive small; PM, positive medium; PL, positive large; PL1, positive large 1; PL2, positive large 2.

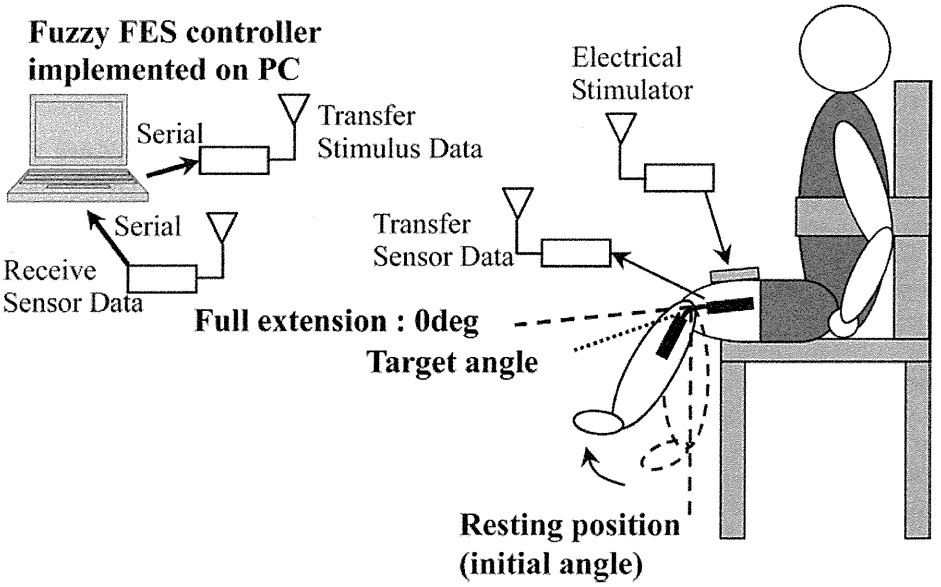

Figure 3. Experimental setup of the knee extension control.

values of fuzzy membership functions for neurologically intact subjects were determined in previous experiments with other subjects [8,9]. The values of fuzzy membership functions for hemiplegic subjects were determined after adjusting their values of neurologically intact subjects from the results of preliminary experiments.

In one experimental session, 100 cycles were performed with neurologically intact subjects, and 35 cycles were performed with hemiplegic subjects to reduce physical load. The knee joint angles were measured with an electric goniometer (M180, Penny & Giles). The output signal of the goniomenter was digitized by a 10 bit A/D converter with 40 Hz of sampling frequency. Pulse width and pulse frequency was fixed at 0.3 ms and 20 Hz, respectively. Stimulus pulse amplitude was determined so as to develop target joint angle without pain before the experiment. Initial value of TB was 0 s.

Results

An example of control results with a hemiplegic subject (Subject C) was shown in figure 4. Stimulation burst duration TB increased as the number of cycles increased, and then the maximum extension angle was reached to the target angle at the 4th control cycle. In the first few cycles, the value of E-OAF was large, which shows the E-OAF worked effectively in early cycles in order to reach the targets with small number of cycles. The value of S-OAF was large at the most cycles, which shows the S-OAF compensated for the weak muscle response of this subject.

For evaluating control results, settling index (SI), mean error (ME) and mean variation (MV) were calculated (table 1). SI was defined as the number of cycles that were required to reach the target joint angle with absolute error that was less than or equal to 3°. ME was mean value of the absolute error between the target angle and the produced maximum extension angle in cycles after reaching the target. MV was mean of the difference in controlled joint angles between two consecutive cycles after reaching the target. The number in parentheses in table 1 shows the result for the first 35 cycles that is the same evaluation condition as the hemiplegic subjects. As seen in table 1, SI was 3–5 cycles, ME was less than 1° for all trials and MV was approximately 1°. The evaluation indices for the hemiplegic subjects showed similar values as those for the neurologically intact subjects.

The developed system performed well in the knee extension control with all subjects. However, there were some cases that the value of S-OAF did not change dynamically to the change in the sensitivity. Figure 5 shows relationship between the sensitivity and the S-OAF of each cycle after reaching the target in the knee extension angle control. The value of sensitivity was about between 20° and 50°/s in the hemiplegic subjects and about between 50° and 90°/s in the neurologically intact subjects. The value of sensitivity in the hemiplegic subjects was small compared to those of neurologically intact subjects, because muscle responses to electrical stimulation were weak with the hemiplegic subjects. The controller used in the experiments adjusted output values (TB) by the S-OAF for subject A (0.7–1.0) and C (1.2–1.5). For Subjects B and D, values of the S-OAF were about 1.0, which shows little adjustment by the S-OAF. The role of the S-OAF is to compensate variation of the muscle properties between subjects, change in muscle response and muscle fatigue. In the control tests, parameter values for the S-OAF were determined based on the previous results [8]. That is, for paralyzed subjects, considering weak muscle responses to electrical stimulation, values of sensitivity for the input membership function (M) were set between 10°/s and 70°/s with 40°/s for the center. Those sensitivity values were similar to those for a neurologically intact subject whose muscle responses were considerably weak [8]. Since the adjustment of the S-OAF was little with one hemiplegic subject and one neurologically intact subject compared with

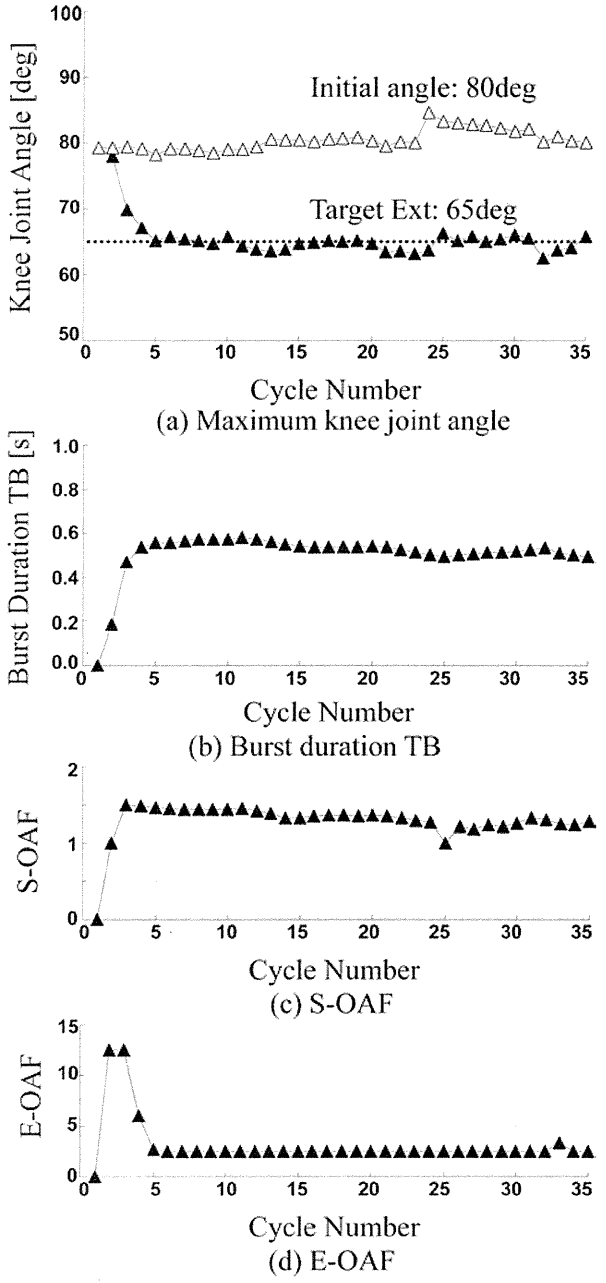

Figure 4. An example of control results of the maximum knee extension angles (Subject C trial 2).

the change in sensitivity, the modification of the S-OAF will be necessary.

Knee flexion and extension control with neurologically intact subjects

Based on the results of the previous section, the range of values of input and output membership functions of the S-OAF were expanded, and the number of terms were increased in order to adapt to changes in these muscle responses. The maximum knee flexion and extension angle control was examined as a sequence of movements stimulating two muscles with

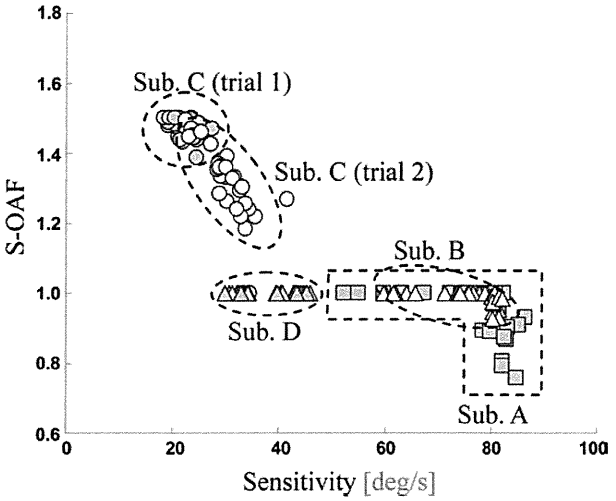

Figure 5. Evaluation results of sensitivity and S-OAF in knee extension angle control.

Table 1. Evaluation results of knee extension control.

Subject range of extension	Max. knee extension control		
	SI (cycle)	ME (deg)	MV (deg)
A 35°	5	0.8 (1.2)	1.0 (1.4)
B 35°	3	0.7 (0.7)	0.9 (1.0)
C 10° (trial 1)	3	0.6	0.8
C 15° (trial 2)	4	0.8	0.8
D 15°	3	0.9	1.0

The number in parentheses shows the result for the first 35 cycles that is the same evaluation condition as the hemiplegic subjects.

neurologically intact subjects because of safety for hemiplegic subjects in positioning during control.

Experimental methods

The maximum knee flexion and extension angles were controlled in one cycle stimulating the hamstrings and the vastus muscles by the surface electrical stimulation system with 7 neurologically intact subjects (figure 6). Subject's consent to participate in the experiment was obtained. The subject sat on the equipment keeping his position by his upper limbs. The initial knee joint angle (neutral position) was approximately 30° and target angles were 45–70° for knee flexion and 10° for extension (the maximum angle of knee extension is defined as 0°). Starting condition for each control cycle was when the difference of knee joint angle between two consecutive cycles is less than 0.3° for the 20 consecutive samples after 6 seconds from the time when the maximum extension angle was detected in the previous control cycle. The hamstrings were stimulated first and then the vastus muscles were stimulated after detecting the maximum flexion angle.

Pulse width was fixed at 0.2 ms. Other electrical stimulation condition and the measurement method of knee joint angle were same as the experiment of knee extension control. Initial value of TB is 0 s and 35 cycles were performed in each control session. Three control sessions were performed for each subject with the time interval between 20 min and 30 min.

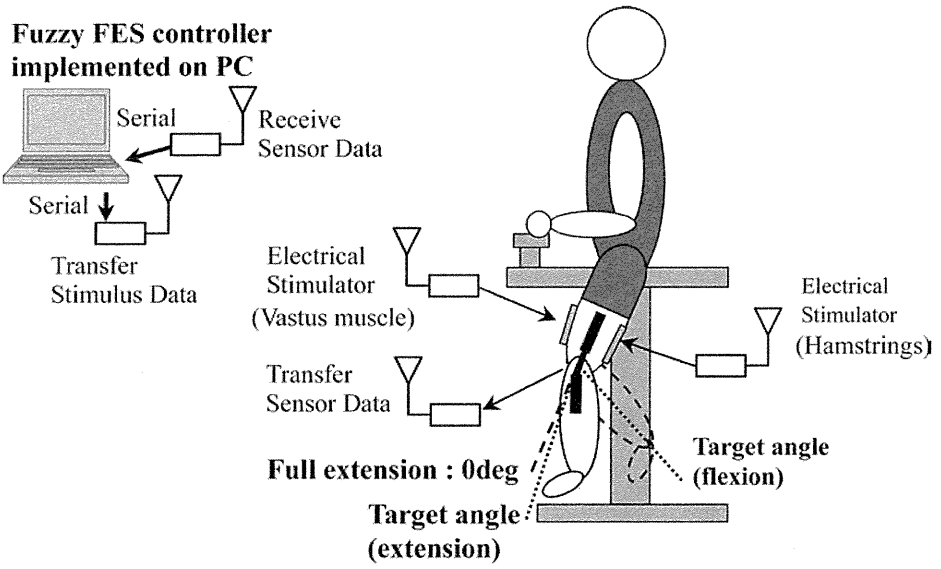

Figure 6. Experimental setup of the knee flexion and extension control.

For the hamstrings, the fuzzy model of the S-OAF was changed to have 7 linguistic terms for input membership function and 7 singletons for the output variable. For the vastus muscles, the fuzzy model of the S-OAF was changed to have 4 linguistic terms for input membership function and 4 singletons for the output variable.

Results

Both maximum joint angles were controlled with five subjects, but sufficient knee flexion angle was not produced by the electrical stimulation with two subjects. One example of control results is shown in figure 7. The maximum flexion and extension angles reached their targets with small number of cycles (3 for the flexion and 4 for the extension, respectively) and were controlled stably during the stimulation cycles after reaching the target. As shown in the case of knee extension control, the E-OAF worked effectively in early cycles and the burst duration was adjusted appropriately by regulating the value of S-OAF (about 1.2 for flexion and about 0.8 for extension, respectively) to compensate for different muscle responses.

For evaluating control results, SI, ME and MV were calculated (table 2). SI was 3–5 cycles, ME was less than 4° for flexion control and less than 2° for extension control. MV was less than 5° for flexion and less than 2.5° for extension.

Discussions

The developed wireless surface electrical stimulation system combined with the fuzzy controller performed well in the knee angle controls. The system realized reaching the target within about 5 cycles. In most of trials, the mean error after reaching the target was less than about 3°, and the mean variation after reaching the target was less than about 3°. These control results were similar to the results in our previous reports [9], which were obtained by using previous wired stimulation system. In addition, under the condition of the longer control cycles than the previous report [9], the maximum knee extension angle was controlled stably with neurologically intact subject. Therefore, the wireless surface electrical stimulation system combined with the fuzzy controller was considered to function effectively as a closed-loop controller.

The developed system worked well with hemiplegic subjects in the knee extension control. Although the muscle response produced by the electrical stimulation with the hemiplegic subjects was weak compared to those of neurologically intact subjects, the ability of fuzzy FES controller based on the cycle-to-cycle control is considered to be appropriate to reach the target angle and to compensate difference in muscle properties between subjects. Therefore, the developed system is expected to be practical in clinical applications.

Stimulation burst duration (TB) was adjusted appropriately, and the knee joint angle was controlled stably by the fuzzy controller with two parameters of the E-OAF and the S-OAF in both control tests. For large error between the control angle and the target angle in early cycles, the E-OAF worked effectively to reach the target with small number of cycles in all subjects. After reaching the target angle, the E-OAF was small because the error of the obtained knee joint angle was small. In contrast, the S-OAF worked to compensate for the different muscle responses during all the stimulus cycles automatically based on the value of sensitivity. These results showed that both of the E-OAF and S-OAF would be effective in controlling the repetitive execution of similar movements for rehabilitation.

In the knee extension angle control, the value of S-OAF did not change dynamically to the change in sensitivity with some subjects. Therefore, the range of values of input and output membership functions of the S-OAF was expanded and the number of terms was increased, and then the knee flexion and extension angle control was examined. Figure 8 shows the sensitivity and the S-OAF of each cycle after reaching the target obtained in the knee flexion and extension angle control. The value of the S-OAF changed dynamically as the sensitivity changed. It may be better to expand the range of the

Table 2. Evaluation results of knee flexion and extension control.

	Max. knee flexion control			Max. knee extension control		
Subject	SI ± SD (cycle)	ME ± SD (deg)	MV ± SD (deg)	SI (cycle) ± SD	ME ± SD (deg)	MV ± SD (deg)
E	4.0±1.0	2.3±0.1	2.9±0.2	3.7±0.6	1.3±0.2	1.2±0.3
F	2.7±0.6	3.3±0.5	3.7±1.1	3.3±0.6	0.9±0.1	1.1±0.2
H	3.0±0.0	1.3±0.2	1.6±0.4	3.0±0.0	0.9±0.2	1.3±0.4
J	4.0±1.0	2.3±1.3	3.4±1.6	2.7±1.6	1.4±0.5	1.7±0.8
K	3.7±0.6	2.1±1.2	2.9±1.7	3.0±0.0	1.5±0.1	2.0±0.1
Average	3.5±0.8	2.3±0.9	2.9±1.2	3.1±0.5	1.2±0.3	1.5±0.5

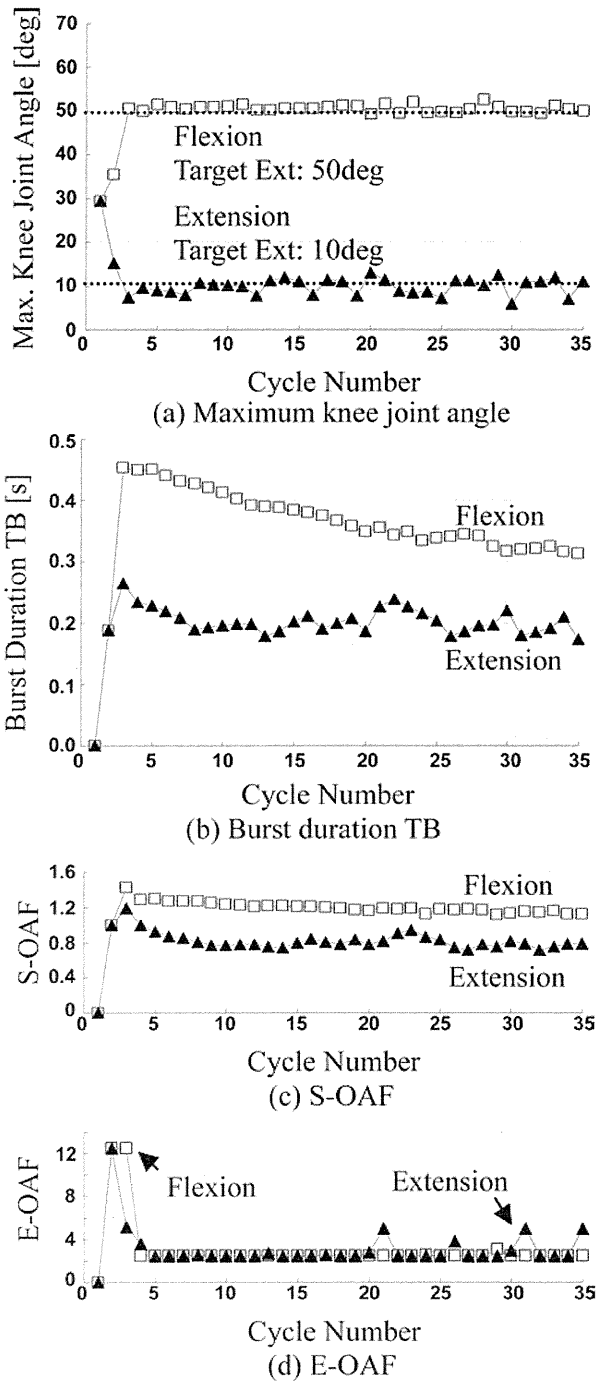

Figure 7. An example of control results of the maximum knee flexion and extension angles (Subj. K, 1st trial).

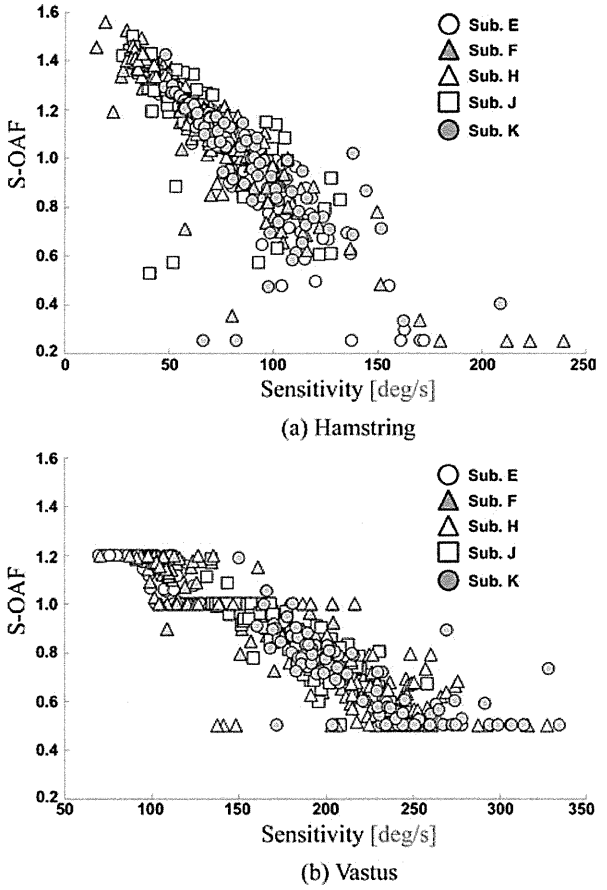

Figure 8. Evaluation results of sensitivity and S-OAF after reaching the target in knee flexion and extension angle control.

input and output membership functions of the S-OAF for the vastus muscles because of the slight saturation of the S-OAF of the vastus muscles in both the lower and higher sensitivity, if necessary.

The S-OAF using the sensitivity, which is the ratio of joint angle change to stimulation burst duration, worked effectively in both hemiplegic subjects and neurologically intact subjects. However, the sensitivity obtained by this method may contain other effects such as movements of other parts of the body or gravitational effect. For optimal movement control, it is required to modify by using directly measured muscle activity such as surface electromyogram elicited by electrical stimulation (M-wave).

The developed wireless surface FES system by using the wireless transceiver module is expected to improve ease of use.

However, the wireless communication has problems such as delay and interference. The delay of wireless communication between the wireless modules used in the developed system was small (2 ms) enough compared to the sampling period of ADC (25 ms) and the stimulus period (50 ms). Therefore, it is considered that the influence of the delay of the wireless communication on the performance of the cycle-to-cycle controller was small in this system. The interference in wireless communication was not caused in the experiments using the wireless transceiver module for the 2.4 GHz (Industrial, Scientific and Medical: ISM) band. However, the interference problem does not always cause in the wireless communication. It is necessary to deal with the problem of the wireless communication by modifying the communication software including time management within each module, the retransmission processing and so on.

The setting of the goniometer for movement measurements is not so easy for rehabilitation training because of limited attachment position and requirement of complicated calibration process. The measurement of movement using wearable sensor such as a gyroscope and accelerometer [14] would be suitable for clinical application of feedback FES control system.

Conclusion

In this study, the small surface electrical stimulator was designed, and then the wireless surface FES system combined with the fuzzy controller based on the cycle-to-cycle control was developed. In order to show the effectiveness of the wireless FES system implemented the fuzzy cycle-to-cycle control for repetitive movement control, the developed wireless FES system was examined in knee joint controls with neurologically intact and hemiplegic subjects. The developed system performed well in the knee joint angle controls adjusting stimulation burst time appropriately as a closed-loop controller with both hemiplegic subjects and neurologically intact subjects, which shows that the wireless FES system can realize stable control. The wireless surface electrical stimulation system would be practical in clinical applications of repetitive execution of similar movements of the limbs for motor rehabilitation with FES.

Declaration of interest: This work was supported in part by the Ministry of Education, Culture, Sports, Science and Technology of Japan under a Grant-in-Aid for Scientific Research (B), and the Saito Gratitude Foundation.

References

[1] Merletti, R., Zelaschi, F., Latella, D., Galli, M., Angeli, S., Sessa, M.B., 1978, A control study of muscle force recovery in hemiparetic patients during treatment with functional electrical stimulation. *Scandinavian Journal of Rehabilitation Medicine*, **10**, 147–154.

[2] Glanz, M., Klawansky, S., Stason, W., Berkey, C., Chalmers, T.C., 1996, Functional electrostimulation in poststroke rehabilitation: a meta-analysis of the randomized controlled trials. *Archives of Physical Medicine and Rehabilitation*, **77**, 549–553.

[3] Yan, T., Hui-Chan, C.W., Li, L.S., 2005, Functional electrical stimulation improves motor recovery of the lower extremity and walking ability of subjects with first acute stroke: a randomized placebo-controlled trial. *Stroke; a Journal of Cerebral Circulation*, **36**, 80–85.

[4] Newsam, C.J., Baker, L.L., 2004, Effect of an electric stimulation facilitation program on quadriceps motor unit recruitment after stroke. *Archives of Physical Medicine and Rehabilitation*, **85**, 2040–2045.

[5] Sheffler, L.R., Chae, J., 2007, Neuromuscular electrical stimulation in neurorehabilitation. *Muscle & Nerve*, **35**, 562–590.

[6] Wirz, M., Zemon, D.H., Rupp, R., Scheel, A., Colombo, G., Dietz, V., Hornby, T.G., 2005, Effectiveness of automated locomotor training in patients with chronic incomplete spinal cord injury: a multicenter trial. *Archives of Physical Medicine and Rehabilitation*, **86**, 672–680.

[7] Arifin, A., Watanabe, T., Hoshimiya, N., 2006, Design of fuzzy controller of the cycle-to-cycle control for swing phase of hemiplegic gait induced by FES. *IEICE Trans Inf & Syst*, E89-D-4, 1525–1533.

[8] Watanabe, T., Masuko, T., Arifin, A., 2008, A feasibility study of fuzzy FES controller based on cycle-to-cycle control: An experimental tes of knee extension control. *IEICE Trans Inf & Syst*, E91-D-3, 865–868.

[9] Watanabe, T., Masuko, T., Arifin, A., 2009, Preliminary tests of a practical fuzzy FES controller based on cycle-to-cycle control in the knee flexion and extension control. *IEICE Trans Inf & Syst*, E92-D-7, 1507–1510.

[10] Veltink, P.H., 1991, Control of FES-induced cyclical movements of the lower leg. *Med & Biol Eng & Comput*, 29, NS8–NS12.

[11] Franken, H.M., Veltink, P.H., Baardman, G., Redmeyer, R.A., Boom, H.B., 1995, Cycle-to-cycle control of swing phase of paraplegic gait induced by surface electrical stimulation. *Medical & Biological Engineering & Computing*, **33**, 440–451.

[12] Burke, R.E., Rudomin, P., Zajac, F.E., 3rd, 1970, Catch property in single mammalian motor units. *Science (New York, N.Y.)*, **168**, 122–124.

[13] Scott, W.B., Lee, S.C., Johnston, T.E., Binkley, J., Binder-Macleod, S.A., 2007, Effect of electrical stimulation pattern on the force responses of paralyzed human quadriceps muscles. *Muscle & Nerve*, **35**, 471–478.

[14] Saito, H., Watanabe, T., 2011, Kalman-filtering-based Joint Angle Measurement with Wireless Wearable Sensor System for Simplified Gait Analysis. *IEICE Trans Inf & Syst*, E94-D (in press).

研究紹介

ナノ・マイクロ加工に基づく人工細胞膜センサの研究

平野愛弓*・大嶋梓*
木村康男**・庭野道夫*,**

細胞膜構造を人工的に構築し，高感度バイオセンサや薬物スクリーニング法として応用しようとする試みは従来から行われてきたが，基本構造となる脂質二分子膜の脆弱性の問題がその発展の障害となってきた．本稿では，半導体微細加工基板やポーラスアルミナナノ構造体を二分子膜の保持体として作製し，その中での膜形成により人工脂質二分子膜の安定性を高めようとする我々の最近のアプローチについて紹介する．

Keywords : bilayer lipid membrane, ion channel, membrane protein, microfabrication, porous alumina, membrane stability, nano-structure

1. まえがき

細胞膜は厚さ数nmのナノ薄膜であり，外界からの化学・光・力学等の刺激に非常に敏感な超高感度センサでもある．その構造はリン脂質分子が二層整列した脂質二分子膜を基本構造とし，そこに種々の膜タンパク質が埋めこまれて構成されている．これらの膜タンパク質は細胞膜の高感度な物質感受性を担っており，創薬の重要なターゲットでもある[1]．細胞膜の基本構造である脂質二分子膜は脂質分子の自己集合により人工的に構築可能であり，この人工脂質二分子膜（人工細胞膜）に精製した膜タンパク質を埋めこんだ膜系は，膜タンパク質の機能や薬物作用を化学組成を制御した上で評価できる系として，生理学・薬理学の分野で広く用いられてきた．一方，膜タンパク質の高度な物質認識能は，高感度バイオセンサの認識素子として注目され[2]，実際にイオンチャネルを用いた脂質二分子膜センサではpM (10^{-12} M (mol/L)) レベルの高感度検出を達成している[3]．このように，人工細胞膜センサは薬物候補化合物の評価や高感度バイオセンサとしての可能性をもつが，膜タンパク質の機能発現にとって必須の環境である脂質二分子膜は安定性が極めて低く，その発展の障壁となってきた．

近年，医薬品の投与により既存の不整脈が増悪したり，新たな不整脈が発生する催不整脈作用の問題から，開発薬物に対する安全性薬理試験として心筋のhERG (human Ether-a-go-go Related Gene) チャネルへの作用評価が必須となり，イオンチャネルに対する高効率な薬物評価系への需要が高まっている[4]．このような社会的背景を受け，2000年以降多くの研究者や企業がチャネル電流計測の分野に参入し，人工細胞膜研究が再び脚光を浴びることとなった．その多くは，成熟した微細加工技術と人工脂質二分子膜形成とを融合することにより，人工脂質二分子膜の課題であった膜安定性や膜形成の再現性を向上させようとするものである[5~7]．本稿では，半導体微細加工やナノ加工技術によって作製したチップ中での膜形成により人工脂質二分子膜を安定化し，イオンチャネルのチップ化を目指す最近のアプローチについて，我々の研究を中心に紹介したい．

2. ナノポーラスアルミナフィルムに基づく脂質二分子膜の安定化

従来，平面脂質二分子膜は，テフロン等の絶縁フィルムに小孔（ϕ：数～数百 μm）をあけ，その中での脂質分子の自己集合によって形成されてきた．プラスチックフィルムにあけた小孔中に脂質溶液を塗布して自発的な二分子膜形成を促す黒膜法（**図1A.(a)**）や，気液界面に形成した脂質分子の単分子膜を小孔内で貼り合わせる単分子膜貼り合わせ法(図1A.(**b**))，ガラスキャピラリーの先端に脂質二分子膜形成を行うチップ-ディップ法（図1A.(**c**)）が古典的な膜形成法として生理学の分野で多く用いられている．

*東北大学大学院医工学研究科　〒980-8579　仙台市青葉区荒巻字青葉6-6.　e-mail : ahirano@bme.tohoku.ac.jp
**東北大学電気通信研究所　〒980-8577　仙台市青葉区片平2-1-1.　e-mail : niwano@riec.tohoku.ac.jp
分類番号　9.4
Artificial cell membrane sensor based on nano- and microfabrication techniques. Ayumi HIRANO-IWATA*, Azusa OSHIMA*, Yasuo KIMURA** and Michio NIWANO*,**.
*Graduate School of Biomedical Engineering, Tohoku University (6-6 Aoba, Aramaki, Aoba-ku, Sendai 980-8579)
**Laboratory for Nanoelectronics and Spintronics, Research Institute of Electrical Communication, Tohoku University (2-1-1 Katahira, Aoba-ku, Sendai 980-8577)

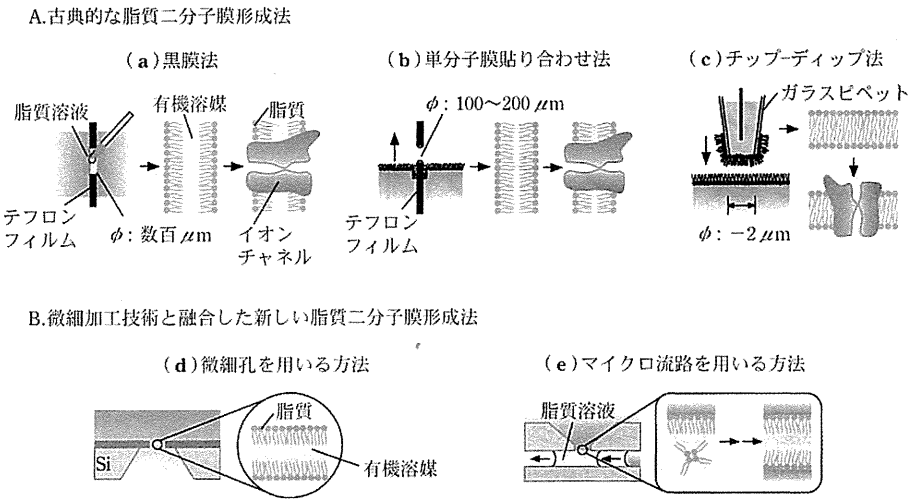

図1　人工細胞膜（人工脂質二分子膜）の形成法.

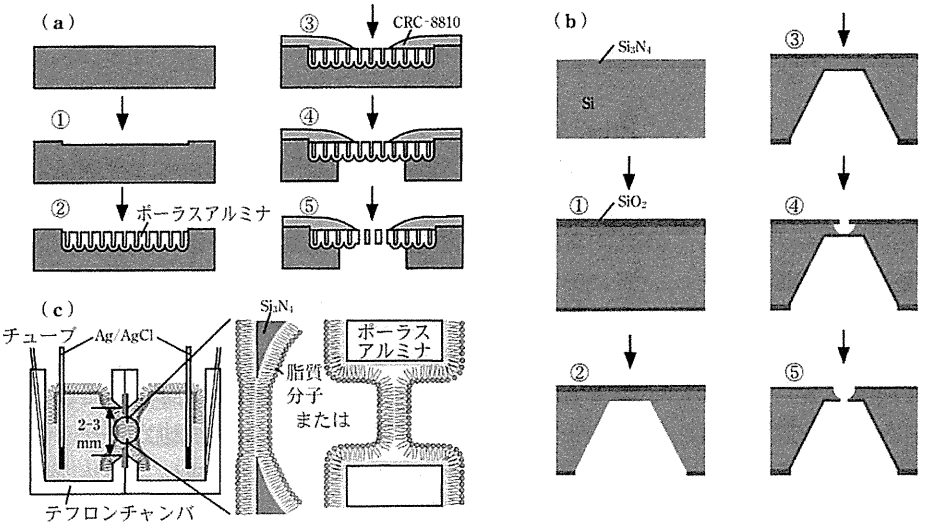

図2　(a)，(b)脂質二分子膜保持体の作製プロセスと(c)二分子膜形成のための実験系．(a)ポーラスアルミナ，①電界研磨，②陽極酸化，③パターニング，④Al層除去，⑤バリア層除去，(b)微細孔を作製したSiチップ，①熱酸化およびスパッタリング，②パターニングと異方性エッチング，③スパッタリング，④等方性エッチング，⑤SiO_2層の除去．(c)テフロンチャンバの真ん中に作製した膜保持体（ポーラスアルミナまたはSiチップ）を装着し，単分子膜貼り合わせ法にて膜形成を行う．膜の両側の各水相にAg/AgCl電極を入れ，電極間に電圧を印加した際に観測される電流値を記録する．

一方，2000年以降，微細加工技術と脂質二分子膜形成を融合する試みが盛んである（図1B.）[2]．これらの研究は，①微細孔を作製して二分子膜の微小化を行い，膜の安定化を目指すもの，②マイクロ流路の利用により，膜形成の簡便化を目指すものの二つに大別され，ともに，高効率薬物スクリーニングへの展開を目指している．しかし，膜形成の簡便化・自動化は進んだものの，膜安定性については寿命の向上のみで，機械的強度の向上には至っていなかった．また，その多くは，不揮発性の有機溶媒を膜形成に用いており，適用可能なチャネルタンパク質の範囲には限界があった．

我々は，脂質二分子膜の形成場となる膜保持体のスケールを二分子膜と同等のnmスケールまで下げることにより脂質二分子膜の安定化が見込めるのではないかと考え，陽極酸化ポーラスアルミナフィルムとシリコン(Si)微細加工基板の二つを二分子膜保持体として作製することを試みた（図2）[8]．これらの微細孔の中での膜形成を行い，両者の膜安定性の比較を行った[9,10]．

陽極酸化ポーラスアルミナは規則的なナノポア構造をもつ絶縁膜であり，その孔径は陽極酸化条件によって制御できる．微小化による二分子膜の安定化を目指すアプローチでは，膜面積の減少に伴ってイオンチャネルの膜への埋め込み確率も低下することが懸念されるが，ポーラスアルミナを保持体として二分子膜形成を行えば，個々の二分子膜が～nmに微小化されるのと同時に，総膜面積は従来と同程度の大きさを維持できる．図2(a)にポーラスアルミナフィルムの作製プロセスを示す．高いアスペクト比(10～20)のポーラスアルミナを用いた場合には二分子膜が形成されなかったため，1～3程度のアスペクト比をもつポーラスアルミナフィルムを作製している．電界研磨したアルミニウム（Al）板をリン酸中で陽極酸化した後，感光性レジストCRC-8810をスピンコートし，フォトリソグラフィにより直径100μmの孔を形成した．Al層を塩酸，硫酸銅混合溶液で除去した後，底面の酸化物層（バリア層）をリン酸溶液で除去して孔形成を行った．作製したポーラスアルミナフィルムはシラン化剤で疎水化処理した後，テフロンチャンバに装着，単分子膜貼り合わせ法による脂質二分子膜形成を行い（図2(c)），膜安定性について寿命，耐電圧性，溶液交換耐性の観点から評価した[9]．

作製したポーラスアルミナは孔径200～350 nm（図3(a)），厚さ0.2～0.5μmであり，このフィルム中では約80％の確率（測定回数$n=101$）でGΩ以上の膜抵抗を示す良好な脂質二分子膜が形成され，ノイズ電流値はピーク幅で1～2 pAであった．この膜系にモデルチャネルのグラミシジンペプチドを添加したところ，グラミシジンの単一チャネル電流を明瞭に記録することができた（図4）．また，

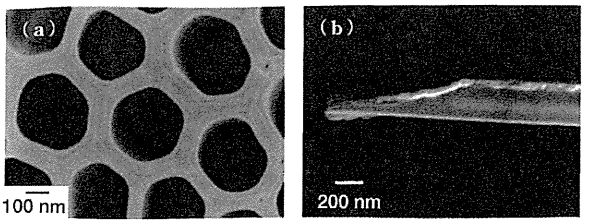

図3　脂質二分子膜保持体のSEM像．(a)ポーラスアルミナ，(b)Siチップ中微細孔のエッジ部分の断面像．

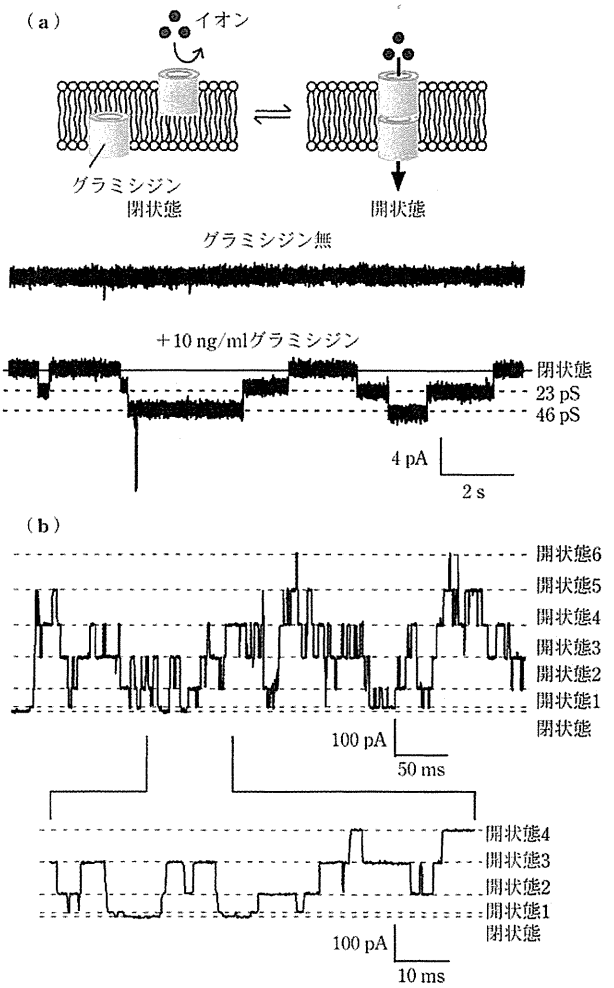

図4　ポーラスアルミナ中で形成した脂質二分子膜を用いて記録した単一チャネル電流．"S"はコンダクタンスの単位，pS＝10^{-12} (1/Ω)．(a)グラミシジン，(b)アラメチシン．(a)の模式図のように，グラミシジンは二分子膜中で二量体会合をすると膜貫通のチャネルを形成し，1価の陽イオンを透過させる．図の電流波形では，このチャネル部分の導電率（pS）の値を記載している．

高速開閉するアラメチシンチャネルの遷移も明瞭に記録できた．これらの結果は，ポーラスアルミナで保持した二分子膜が，高い生体膜類似性と，生体チャネルのチャネル電流記録に適した電気特性とを兼ね備えていることを示している．この膜系は±1Vの印加電圧耐性と膜寿命16時間を示し，従来の二分子膜（崩壊電圧：0.3～0.5 V[11,12]，寿命：数時間[13]）に比べて高い膜安定性を示した．しかし，薬物スクリーニングへの応用では必須となる溶液交換耐性は

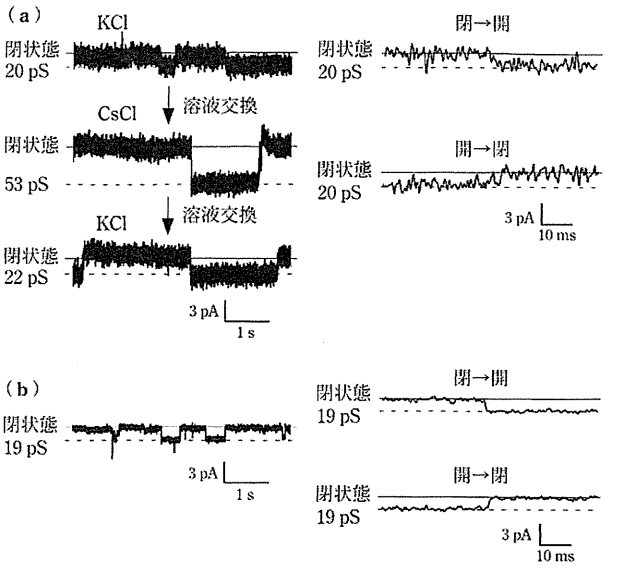

図5　Siチップ中で形成した脂質二分子膜を用いて記録した単一チャネル電流．(a)絶縁層被覆無し，(b)絶縁層被覆有り．右側は，チャネル開閉時の波形の拡大図．

得られなかった．

3.　半導体微細加工に基づく脂質二分子膜の安定化 —微細孔のエッジ形状に基づく安定化

上述のポーラスアルミナの経験により，二分子膜の微小化では十分な膜安定性が得られないことがわかってきた．そこで我々は，微細孔のエッジと二分子膜との接合部の形状に注目し，滑らかなエッジを持つような微細孔を半導体微細加工によりSi_3N_4/Si基板中に作製し(図2(b))，その中での脂質二分子膜形成を試みた[10]．このチップは，十分な膜面積を保持できる孔径（20～30 μm）をもち，小孔のエッジはnmスケールでテーパーの付いた滑らかな形状（図3(b)）となるように設計した．厚さ240 nmのSi_3N_4を積層したSi基板中に，フォトリソグラフィ，ウェットエッチングにより微小孔を作製し，疎水化処理の後膜形成を行った．

作製したSiチップ中での脂質二分子膜形成を検討したところ，90% を超える確率（n＝53）でGΩ以上の膜抵抗を示す二分子膜が形成された．この二分子膜の安定性は高く，±1V以上の耐電圧性と寿命15～45時間（n＝5）を示した．また，薬物スクリーニングへの応用では必須となる溶液交換耐性も兼ね備えており，同一の膜に対して水溶液組成をKCl→CsCl→KClと交換した際のグラミシジンチャネル電流を単一チャネルレベルで記録することに成功した（図5(a)）．この結果は，複数回の溶液交換に耐える機械的強度の高い二分子膜系の構築に成功したことを意味する．その一方で，この二分子膜の電気特性上の問題も判明した．Siチップ中で形成した二分子膜の場合は，二分子膜とチップの総電気容量が大きく，ノイズ電流が大きくなってしまう．また，大きな電気容量は過渡応答の要因となるため，生体チャネルの高速（～ms）な開閉に測定が追

随できない可能性があることがわかった．そこで，作製したSiチップをSiO_2熱酸化膜とテフロン層で被覆することにより膜系全体の総電気容量の抑制を行った結果，ノイズ電流値を1～2 pA(ピーク電流幅)，過渡応答を1 ms以下にまで抑制することに成功した（図5(**b**)）[14]．これは，生体チャネルの単一チャネル電流記録に適した電気特性であり，今後の生体チャネルへの展開が期待される．また，我々の二分子膜では膜形成に必要な有機溶媒量は10 nLにまで減じており，脆弱なチャネルも含む幅広いチャネルタンパク質に適用可能であり，その応用可能性は高いと考えている．

4. むすび

微細加工技術との融合により，脂質二分子膜は安定性，操作性ともに著しく向上した．今後の研究は，グラミシジンのようなモデルチャネルではなく，薬物評価の対象として重要な，あるいはセンサ素子として有用なチャネルタンパク質を，このような新しい二分子膜系にいかに効率よく埋めこみ，イオンチャネルチップとして発展させていくかに焦点が移っていくであろう．昆虫細胞による大量発現系や無細胞タンパク質合成系の進歩により，膜タンパク質の操作性が確実に向上していく今，イオンチャネルチップが実現される日も近いと信じている．

文　献

1) J. P. Overington, B. Al-Lazikani, and A. L. Hopkins: Nat. Rev. Drug Discov. **5**, 993 (2006).
2) A. Hirano-Iwata, M. Niwano, and M. Sugawara: Trends Anal. Chem. **27**, 512 (2008).
3) M. Sugawara, A. Hirano, M. Rehák, J. Nakanishi, K. Kawai, H. Sato, and Y. Umezawa: Biosens. Bioelectron. **12**, 425 (1997).
4) 小林　力：日薬理誌 (Folia Pharmacol. Jpn) **128**, 369 (2006).
5) C. Schmidt, M. Mayer, and H. Vogel: Angew. Chem. Int. Ed. **39**, 3137 (2000).
6) N. Fertig, M. George, M. Klau, C. Meyer, A. Tilke, C. Sobotta, R. H. Blick, and J. C. Behrends: Receptors Channels **9**, 29 (2003).
7) 竹内昌治：表面科学 **29**, 370 (2008).
8) A. Hirano-Iwata, A. Oshima, T. Nasu, T. Taira, Y. Kimura, and M. Niwano: Supramol. Chem. **22**, 405 (2010).
9) A. Hirano-Iwata, T. Taira, A. Oshima, Y. Kimura, and M. Niwano: Appl. Phys. Lett. **96**, 213706 (2010).
10) A. Hirano-Iwata, K. Aoto, A. Oshima, T. Taira, R. Yamaguchi, Y. Kimura, and M. Niwano: Langmuir **26**, 1949 (2010).
11) M. Mayer, J. K. Kriebel, M. T. Tosteson, and G. M. Whitesides: Biophys. J. **85**, 2684 (2003).
12) J. W. Shim and L. Q. Gu: Anal. Chem. **79**, 2207 (2007).
13) M. C. Peterman, J. M. Ziebarth, O. Braha, H. Bayley, H. A. Fishman, and D. M. Bloom, Biomed. Microdev. **4**, 231 (2002).
14) A. Oshima, A. Hirano-Iwata, T. Nasu, Y. Kimura, and M. Niwano, Micro and Nanosystems. 印刷中.

(2011年9月1日　受理)

平野　愛弓（ひらの　あゆみ）

1998年東京大学大学院理学系研究科博士課程修了．博士(理学)．98年日本学術振興会特別研究員PD，00年日本大学文理学部助手，03年日本学術振興会海外特別研究員，06年東北大学電気通信研究所助手，08年より同大大学院医工学研究科准教授．研究分野：イオンチャネルを用いたバイオチップの開発，脳機能計測法の開発．

大嶋　梓（おおしま　あずさ）

2010年東北大学大学院医工学研究科修士課程修了．10年より同大大学院博士課程在学中．研究分野：半導体微細加工に基づくイオンチャネルセンサの開発．

木村　康男（きむら　やすお）

1999年東京大学大学院工学系研究科博士課程修了．博士（工学）．99年東北大学電気通信研究所助手，10年より同准教授．研究分野：ナノ構造体形成技術の開発とそのナノデバイスへの応用．

庭野　道夫（にわの　みちお）

1980年東北大学大学院理学研究科博士課程修了．理学博士．80年宮城教育大学助手，87年東北大学電気通信研究所助手，89年同助教授を経て，98年より同教授．研究分野：ナノデバイスの開発とバイオ・環境分野への応用．

Society For Biomaterials

Preparation, structure, and *in vitro* chemical durability of yttrium phosphate microspheres for intra-arterial radiotherapy

Masakazu Kawashita,[1] Naoko Matsui,[1] Zhixia Li,[1] Toshiki Miyazaki,[2] Hiroyasu Kanetaka[1]

[1]Department of Biomedical Engineering, Graduate School of Biomedical Engineering, Tohoku University, Aoba-ku, Sendai 980-8579, Japan

[2]Department of Biological Functions and Engineering, Graduate School of Life Science and Systems Engineering, Kyushu Institute of Technology, Wakamatsu-ku, Kitakyushu 808-0196, Japan

Received 7 February 2011; revised 19 April 2011; accepted 20 April 2011
Published online 28 June 2011 in Wiley Online Library (wileyonlinelibrary.com). DOI: 10.1002/jbm.b.31870

Abstract: Chemically durable microspheres containing yttrium and/or phosphorus are useful for intra-arterial radiotherapy. In this study, we attempted to prepare yttrium phosphate (YPO_4) microspheres with high chemical durability. YPO_4 microspheres with smooth surfaces and diameters of around 25 μm were successfully obtained when gelatin droplets containing yttrium and phosphate ions were cooled and solidified in a water-in-oil emulsion and then heat-treated at 1100°C. The chemical durability of the heat-treated microspheres in a simulated body fluid at pH = 6 and 7 was high enough for clinical application of intra-arterial radiotherapy. © 2011 Wiley Periodicals, Inc. J Biomed Mater Res Part B: Appl Biomater 99B: 45–50, 2011.

Key Words: yttrium phosphate, chemical durability, microspheres, intra-arterial radiotherapy

How to cite this article: Kawashita M, Matsui N, Li Z, Miyazaki T, Kanetaka H. 2011. Preparation, structure, and *in vitro* chemical durability of yttrium phosphate microspheres for intra-arterial radiotherapy. J Biomed Mater Res Part B 2011:99B:45–50.

INTRODUCTION

Intra-arterial radiotherapy of malignant liver tumors has been performed using radioactive yttrium-containing microspheres.[1,2] Yttrium-89 (^{89}Y) is a nonradioactive isotope with a natural abundance of 100%; neutron bombardment activates ^{89}Y to form the β-emitter ^{90}Y, which has a half-life of 64.1 h. When radioactive microspheres 20–35 μm in diameter are injected into a target organ, they are trapped inside small blood vessels in the tumor, blocking the nutritional supply to the tumor and delivering a large, localized dose of short-range, highly ionizing β-rays. The β-rays penetrate only about 2.5 mm in living tissue, thus causing little radiation damage to neighboring healthy tissues. These microspheres show high chemical durability, and the radioactive ^{90}Y remains essentially within the microspheres and does not affect neighboring healthy tissues. The radioactivity of ^{90}Y decays to a negligible level within 21 days after neutron bombardment. Therefore, the microspheres become inactive soon after the cancer treatment.

So far, Y_2O_3–Al_2O_3–SiO_2 (YAS) glass microspheres (TheraSphere®)[3–5] and yttrium-containing resin microspheres (SIR-Spheres®)[6–8] have yielded good results in clinical trials.[9–12] They have been used clinically to treat metastatic liver carcinoma and unresectable hepatocellular carcinoma in various countries including the United States, Canada, China, Australia, New Zealand, Singapore, and European countries.[13–28] The Y_2O_3 content in TheraSphere® is 17 mol %,[29] and the yttrium content in SIR-Spheres® is speculated to be small because SIR-Spheres® have relatively low specific radioactivity around 50 Bq/microsphere compared with TheraSphere® (around 2500 Bq/microsphere).[16,26] The radioactivity of these microspheres decays significantly even before cancer treatment is started because of the short half-life. Therefore, the development of chemically durable microspheres having a higher yttrium content is desirable. We have developed dense Y_2O_3 microspheres,[30] hollow Y_2O_3 microspheres,[31] and porous Y_2O_3 microparticles[32] with high chemical durability *in vitro*.

On the other hand, phosphorus-31 (^{31}P), found at a natural abundance of 100%, can also be activated by neutron bombardment to form the β-emitter ^{32}P, which has a half-life of 14.3 days. Microspheres containing a high phosphorus content are therefore expected to be effective for cancer treatment, similar to yttrium-containing microspheres.[33,34] Previously, we attempted to prepare yttrium phosphate (YPO_4) microspheres by a high-frequency induction thermal plasma melting method and found that they showed high chemical durability *in vitro*.[30] However, they lost a certain amount of phosphorus to form Y_2O_3, and their surfaces were rather rough owing to the loss of phosphorus from volatilization at the higher synthesis temperatures (above 10,000°C). It is feared that the rough surfaces of the microspheres would damage blood vessels. In this study, we attempted to prepare YPO_4 microparticles with a

Correspondence to: M. Kawashita; e-mail: m-kawa@ecei.tohoku.ac.jp
Contract grant sponsor: Japan Society for the Promotion of Science; contract grant number: 22300163.
Contract grant sponsor: The Ministry of Education, Culture, Sports, Science and Technology, Japan

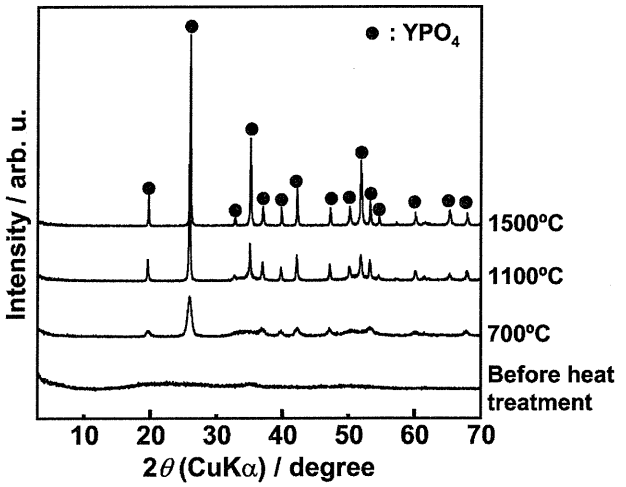

FIGURE 1. XRD patterns of samples before and after heat treatment at different temperatures.

smooth surface and investigated their structure and *in vitro* chemical durability to evaluate their potential as a radioactive source in intra-arterial radiotherapy.

MATERIALS AND METHODS

Sample preparation

A precursor precipitate containing yttrium and phosphate ions was obtained by the following solution precipitation process.[35] Equimolar (8.4 m*M*) amounts of yttrium nitrate ($Y[NO_3]_3$: Wako Pure Chemical Industries, Osaka, Japan) and phosphoric acid (H_3PO_4: Wako Pure Chemical Industries, Osaka, Japan) were dissolved in 300 mL of pure water. Aqueous NaOH solution (56 m*M*, 150 mL) was added to the $Y(NO_3)_3$–H_3PO_4 solution under stirring for 20 min, resulting in an opaque solution. This opaque solution was centrifuged at 4000 rpm for 5 min and decanted to obtain white precipitates. The precipitates were washed several times with pure water. Then, 2.5 mL of 0.1*M* nitric acid aqueous solution was added to 10 g of the white precipitates to obtain a stable sol solution.[36] Gelatin (0.5 g; APH-250, Nitta Gelatin, Osaka, Japan) was dissolved in 5 mL of the sol solution. The resultant solution was dropped into 50 mL of corn oil (Wako Pure Chemical Industries, Osaka, Japan) at 30°C and stirred at 1000 rpm for 10 min to obtain a water-in-oil emulsion. The emulsion was cooled in an ice bath to solidify the gelatin-containing water droplets. The solidified droplets were filtered and washed with cold ethanol and then freeze-dried for 6 h in a freeze dryer (FD-1000; Tokyo Rikakikai Co., Tokyo, Japan). Finally, the freeze-dried samples were placed in an alumina boat, heated to various temperatures (700–1500°C) at a rate of 5°C/min in a SiC or $MoSi_2$ electric furnace, and kept at the given temperature for 1 h.

Structural analysis

The shapes of the microspheres were observed using a scanning electron microscope (SEM; VE-8800, Keyence, Tokyo, Japan). The precipitated phase was examined with a powder X-ray diffractometer (XRD; RINT-2200VL, Rigaku Co., Tokyo, Japan) using the following settings: X-ray source, Ni-filtered CuKα radiation; X-ray power, 40 kV, 40 mA; scanning rate, 2θ = 2°/min; and sampling angle, 0.02°. The structure of the heat-treated microspheres before and after an *in vitro* chemical durability test was investigated by Fourier-transform infrared spectroscopy (FT-IR; FT/IR-6200, JASCO, Tokyo, Japan) with a diffusive reflection attachment (DR-PRO410M, JASCO, Tokyo, Japan). For the FT-IR diffusive reflection spectroscopic measurement, potassium bromide (KBr) powder was mixed with the samples. The sample content in KBr pellets was around 0.5 wt %.

In vitro chemical durability test

A simulated body fluid (SBF) with ion concentrations of Na^+ 142.0, K^+ 5.0, Mg^{2+} 1.5, Ca^{2+} 2.5, Cl^- 147.8, HCO_3^- 4.2, HPO_4^{2-} 1.0, and SO_4^{2-} 0.5 m*M* was prepared by dissolving reagent-grade NaCl, $NaHCO_3$, KCl, $K_2HPO_4{\cdot}3H_2O$, $MgCl_2{\cdot}6H_2O$, $CaCl_2$, and Na_2SO_4 (Nacalai Tesque, Kyoto, Japan) in ultrapure water and buffering to pH 7.40 with tris(hydroxymethyl) aminomethane ($[CH_2OH]_3CNH_2$) and 1*M* HCl (Nacalai Tesque, Kyoto, Japan) at 36.5°C.[37] Then, the pH value of the SBF was adjusted to 6 (SBF-6) or 7 (SBF-7) by further addition of 1*M* HCl.

The microspheres (0.025 g) heat-treated at 1100°C were soaked in 10 mL of SBF-6 or SBF-7 in a polypropylene bottle at 36.5°C for various periods up to 21 days. The pH value of a normal body fluid is maintained at around pH 7, but this value is liable to fall to around pH 6 near a cancer

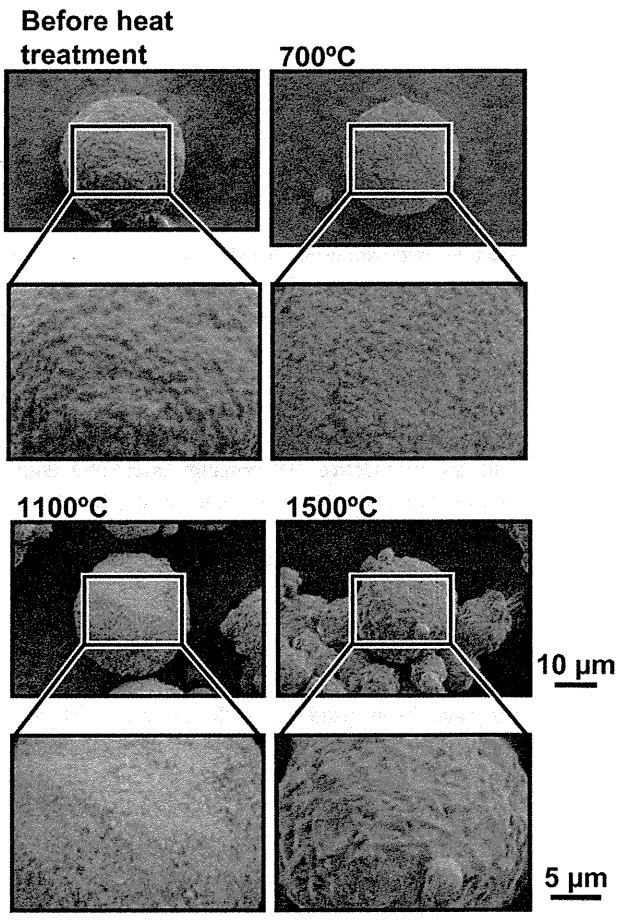

FIGURE 2. SEM photographs of samples before and after heat treatment at different temperatures.